

Constraining the phase shift of relativistic species in DESI BAOs

Abbé M. Whitford,¹ Hugo Rivera-Morales,^{2*} Cullan Howlett,¹ Mariana Vargas-Magaña,² Sébastien Fromenteau,³ Tamara M. Davis,¹ Alejandro Pérez-Fernández,⁴ Arnaud de Mattia,⁵ Steven Ahlen,⁶ Davide Bianchi,⁷ David Brooks,⁸ Etienne Burtin,⁵ Todd Claybaugh,⁹ Axel de la Macorra,² Peter Doel,⁸ Simone Ferraro,^{10,9} Jaime E. Forero-Romero,^{11,12} Enrique Gaztañaga,^{15,13,14} Satya Gontcho A Gontcho,⁹ Gaston Gutierrez,¹⁶ Stephanie Juneau,¹⁷ Robert Kehoe,¹⁸ David Kirkby,¹⁹ Theodore Kisner,⁹ Sergey Kopusov,^{20,21} Martin Landriau,⁹ Laurent Le Guillou,²² Aaron Meisner,¹⁷ Ramon Miquel,^{24,23} Francisco Prada,²⁵ Ignasi Pérez-Ràfols,²⁶ Graziano Rossi,²⁷ Eusebio Sanchez,²⁸ Michael Schubnell,^{30,29} David Sprayberry,¹⁷ Gregory Tarlé,³⁰ Benjamin Alan Weaver,¹⁷ Pauline Zarrouk,²² Hu Zou³¹

¹School of Mathematics and Physics, University of Queensland, Brisbane, QLD 4072, Australia

²Universidad Nacional Autónoma de México. Instituto de Física. A.P. 20-364, 01000. Cd. de México, México

³Universidad Nacional Autónoma de México. Instituto de Ciencias Físicas, 62210, Cuernavaca, Morelos, México

⁴Max Planck Institute for Extraterrestrial Physics, Gießenbachstraße 1, 85748 Garching, Germany

⁵IRFU, CEA, Université Paris-Saclay, F-91191 Gif-sur-Yvette, France

⁶Physics Dept., Boston University, 590 Commonwealth Avenue, Boston, MA 02215, USA

⁷Dipartimento di Fisica “Aldo Pontremoli”, Università degli Studi di Milano, Via Celoria 16, I-20133 Milano, Italy

⁸Department of Physics & Astronomy, University College London, Gower Street, London, WC1E 6BT, UK

⁹Lawrence Berkeley National Laboratory, 1 Cyclotron Road, Berkeley, CA 94720, USA

¹⁰University of California, Berkeley, 110 Sproul Hall #5800 Berkeley, CA 94720, USA

¹¹Departamento de Física, Universidad de los Andes, Cra. 1 No. 18A-10, Edificio Ip, CP 111711, Bogotá, Colombia

¹²Observatorio Astronómico, Universidad de los Andes, Cra. 1 No. 18A-10, Edificio H, CP 111711 Bogotá, Colombia

¹³Institut d’Estudis Espacials de Catalunya (IEEC), c/ Esteve Terradas 1, Edifici RDIT, Campus PMT-UPC, 08860 Castelldefels, Spain

¹⁴Institute of Cosmology and Gravitation, University of Portsmouth, Dennis Sciama Building, Portsmouth, PO1 3FX, UK

¹⁵Institute of Space Sciences, ICE-CSIC, Campus UAB, Carrer de Can Magrans s/n, 08913 Bellaterra, Barcelona, Spain

¹⁶Fermi National Accelerator Laboratory, PO Box 500, Batavia, IL 60510, USA

¹⁷NSF NOIRLab, 950 N. Cherry Ave., Tucson, AZ 85719, USA

¹⁸Department of Physics, Southern Methodist University, 3215 Daniel Avenue, Dallas, TX 75275, USA

¹⁹Department of Physics and Astronomy, University of California, Irvine, 92697, USA

²⁰Institute for Astronomy, University of Edinburgh, Royal Observatory, Blackford Hill, Edinburgh EH9 3HJ, UK

²¹Institute of Astronomy, University of Cambridge, Madingley Road, Cambridge CB3 0HA, UK

²²Sorbonne Université, CNRS/IN2P3, Laboratoire de Physique Nucléaire et de Hautes Energies (LPNHE), FR-75005 Paris, France

²³Institució Catalana de Recerca i Estudis Avançats, Passeig de Lluís Companys, 23, 08010 Barcelona, Spain

²⁴Institut de Física d’Altes Energies (IFAE), The Barcelona Institute of Science and Technology, Edifici Cn, Campus UAB, 08193, Bellaterra (Barcelona), Spain

²⁵Instituto de Astrofísica de Andalucía (CSIC), Glorieta de la Astronomía, s/n, E-18008 Granada, Spain

²⁶Departament de Física, EEBE, Universitat Politècnica de Catalunya, c/Eduard Maristany 10, 08930 Barcelona, Spain

²⁷Department of Physics and Astronomy, Sejong University, 209 Neungdong-ro, Gwangjin-gu, Seoul 05006, Republic of Korea

²⁸CIEMAT, Avenida Complutense 40, E-28040 Madrid, Spain

²⁹Department of Physics, University of Michigan, 450 Church Street, Ann Arbor, MI 48109, USA

³⁰University of Michigan, 500 S. State Street, Ann Arbor, MI 48109, USA

³¹National Astronomical Observatories, Chinese Academy of Sciences, A20 Datun Rd., Chaoyang District, Beijing, 100012, P.R. China

Accepted XXX. Received YYY; in original form ZZZ

ABSTRACT

In the early Universe, neutrinos decouple quickly from the primordial plasma and propagate without further interactions. The impact of free-streaming neutrinos is to create a temporal shift in the gravitational potential that impacts the acoustic waves known as baryon acoustic oscillations (BAOs), resulting in a non-linear spatial shift in the Fourier-space BAO signal. In this work, we make use of and extend upon an existing methodology to measure the phase shift amplitude β_ϕ and apply it to the DESI Data Release 1 (DR1) BAOs with an anisotropic BAO fitting pipeline. We validate the fitting methodology by testing the pipeline with two publicly available fitting codes applied to highly precise cubic box simulations and realistic simulations representative of the DESI DR1 data. We find further study towards the methods used in fitting the BAO signal will be necessary to ensure accurate constraints on β_ϕ in future DESI data releases. Using DESI DR1, we present individual measurements of the anisotropic BAO distortion parameters and the β_ϕ for the different tracers, and additionally a combined fit to β_ϕ resulting in $\beta_\phi = 2.7 \pm 1.7$. After including a prior on the distortion parameters from constraints using *Planck* we find $\beta_\phi = 2.7^{+0.60}_{-0.67}$ suggesting $\beta_\phi > 0$ at 4.3σ significance. This result may hint at a phase shift that is not purely sourced from the standard model expectation for N_{eff} or could be a upwards statistical fluctuation in the measured β_ϕ ; this result relaxes in models with additional freedom beyond Λ CDM.

Key words: large-scale structure of Universe – neutrinos – astroparticle physics – cosmology: observations – cosmology: theory – cosmology: cosmological parameters

1 INTRODUCTION

The present-day distribution of matter perturbations in the Universe has grown from the over and under-densities that froze in place when sound waves in the early Universe ceased to propagate. These sound waves are called the BAOs, and could propagate in the hot and dense plasma at early times due to the coupling between baryons and photons. At the epoch of recombination at $z \sim 1090$, photons were no longer energetic enough to ionize atoms, and photons began decouple from the baryons and stream freely; these photons are measured today as the cosmic microwave background (CMB, [Penzias & Wilson 1979](#)). The BAOs ceased to propagate completely at the baryon drag epoch at which baryons and photons completely decoupled.

In the present day, galaxies throughout the Universe trace the underlying matter distribution; galaxy surveys such as the Dark Energy Spectroscopic Instrument (DESI, [Aghamousa et al. 2016](#)) aim to probe the large-scale distribution of galaxies to measure the imprint of the BAOs and test models of cosmology. This has already been probed by various surveys ([Cole et al. 2005](#); [Eisenstein et al. 2005](#); [Gil-Marín et al. 2016](#); [Abbott et al. 2019](#)) and most recently in DESI data ([Moon et al. 2023](#); [Adame et al. 2024a,b](#)) who have measured the ‘peak’ in the two-point auto-correlation function of galaxies or the ‘wiggles’ that can be seen due to this peak in Fourier space (the Fourier-space transform is referred to as the power spectrum). The peak corresponds to the BAO scale r_s ; the longest distance sound waves could travel up until the baryon drag epoch and also represents a separation scale at which there is an excess probability of finding pairs of galaxies.

Historically, the BAO peak is used to test cosmological models in a partially model-independent way; by measuring a parameter α that represents a ratio of distance scales in an fiducial cosmological model (used to convert the galaxy catalogue angular coordinates and redshifts into Cartesian coordinates) to the same distance scales in the true cosmology. If the fiducial cosmology matches the truth, the parameter α is unity; if not, deviations from unity occur as the physical BAO scale and the BAO scale of the fiducial cosmology do not match. The scaling of the parameter α physically represents an isotropic scaling or distortion of the distance to the BAO peak ([Bernal et al. 2020](#)).

The BAO analysis can be extended to additionally account for anisotropic distortions, which are described by the Alcock-Paczynski (AP, [Alcock & Paczyński 1979](#)) effect. In essence, the difference between the assumed fiducial cosmology model and the true cosmology distorts the distribution of galaxies in the sky differently in directions transverse or parallel to the line-of-sight ([Bernal et al. 2020](#)). The effect arises due to transforming the redshift-space co-ordinates of objects to real-space coordinates, and the distortions are more significant at higher redshift. In the anisotropic analysis, an additional scaling parameter α_{AP} can be measured, representing the anisotropic elongation or compression of the BAO.¹ Depending on the constraining power of the data available, it may only be possible to measure the α parameter using the isotropic fitting methodology. That is, if only the monopole multipole (the first $\ell = 0$ term in the Legendre expansion of the anisotropic power spectrum corresponding to the spherically isotropic component) of the galaxy power spectrum is constrained by the data. If the quadrupole multipole ($\ell = 2$) is constrained this contains more information about the shape of the

¹ It is also common to change variables from α and α_{AP} to α_{\parallel} and α_{\perp} , which represent the scaling of the BAO parallel and transverse to the line-of-sight respectively. A simple transformation exists between the two bases, which we present in Section 2.

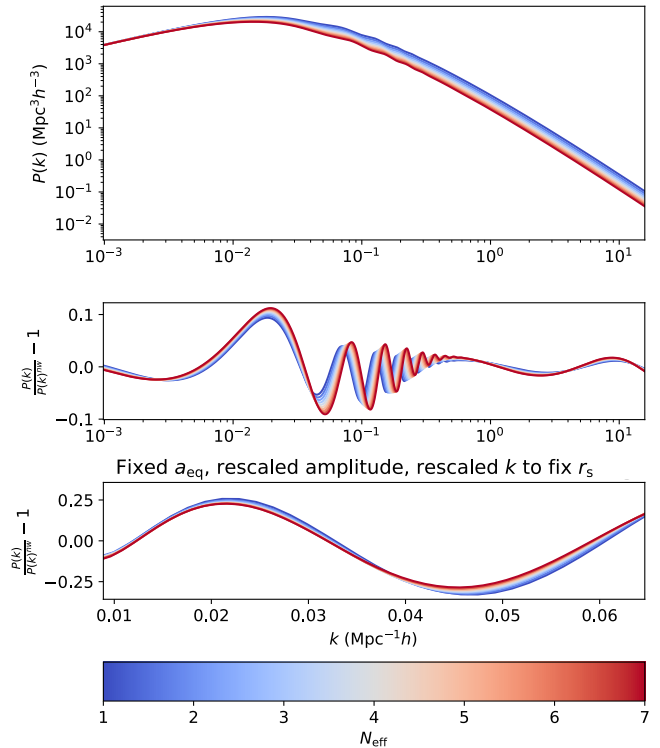


Figure 1. This figure has been inspired by Figure 3 in [Baumann et al. \(2018\)](#). The top panel shows the effect of altering N_{eff} on the matter power spectrum, while the middle panel shows the ratio of the power spectrum plotted to a de-wiggled (smooth) power spectrum; all other cosmological parameters are held fixed. The power spectrum has been calculated using the Boltzmann solver CLASS ([Blas et al. 2011](#)), and smoothed to isolate the wiggles using the method in [Hinton et al. \(2016\)](#). Altering N_{eff} has several notable effects: 1) it alters the amplitude of the BAO wiggles because the ratio of radiation to baryonic matter is changed and this affects the amplitude of rarefactions and compressions in the BAO sound waves; 2) the amplitude of the spectrum for k -modes that entered the horizon before the epoch of matter-radiation equality are suppressed by increasing N_{eff} because the additional radiation density suppresses structure growth of these modes during the era that radiation dominates the expansion rate; and 3) additional radiation alters the position of the peaks and the large turnover by increasing the expansion rate, which allows the epoch of matter-radiation equality and recombination to occur at an earlier time; the scales are smaller than in a Universe that takes longer to reach these epochs. In the lowest panel these effects have been removed to isolate the effect of N_{eff} on only the phase of the BAO wiggles. This is done by calculating the power spectrum wiggles as in the middle panel, but with various differences. When altering N_{eff} we also alter Ω_m such that $\alpha_{\text{eq}} = \frac{\Omega_r}{\Omega_m}$ is held fixed. For each model with different N_{eff} and Ω_m , we rescale the k modes plotted on the x -axis by the ratio of r_s^f and the model r_s (where f is a fiducial model with $N_{\text{eff}} = 3.044$, $\Omega_m = 0.315$) so that the impact of the changing r_s is effectively removed. Finally, the amplitude of the wiggles is rescaled so that there is a fixed maximum height for any of the peaks shown.

power spectrum anisotropy and enough information to measure α and α_{AP} in an anisotropic fit. The fits to the values of α and α_{AP} can eventually be turned into constraints on cosmological parameters or models, or combined with other datasets such as *Planck* ([Aghanim et al. 2020](#)) to improve constraints on the matter density Ω_m and the expansion rate H_0 . As various cosmological parameters that change the expansion rate will have degenerate effects on α and α_{AP} , the distortion parameters may require measurements in several redshift bins to obtain useful constraints on cosmological parameters.

The majority of analyses to this date have not taken into account an additional piece of information that the imprint of the BAOs in galaxy surveys may give us about light relics in the early Universe. Bashinsky & Seljak (2004) first showed that free-streaming neutrinos (or any light relics that free-stream) with a speed faster than the sound speed in the early Universe induce a shift in the phase of the BAO wiggles that can be seen in Fourier space. This phase shift can be understood in that as neutrinos propagate after decoupling from the primordial plasma, they alter the gravitational potential that influences it by carrying away energy. This alteration of the potential induced a temporal shift in the BAO sound waves, that consequently led to a shift in the scale at which the sound waves froze in place and seeded the Large-scale Structure we see today. The phase shift is also discussed in detail in Baumann et al. (2016). Under the assumption that the primordial fluctuations are adiabatic, this phase shift is not degenerate with any other parameters and is a unique signature of neutrinos. Even if there were non-adiabatic primordial fluctuations, the scale dependence of the phase shift may still possibly allow it to be distinguished from non-adiabatic fluctuations (Baumann et al. 2018).

The phase shift was first parameterized and measured in CMB data from the *Planck* satellite by Follin et al. (2015), whose analysis showed a probability $p = 8 \times 10^{-6}$ for the absence of a phase shift due to free-streaming relics, indicating a strong presence of free-streaming relics. More recently, it was parameterized and measured in BAO data from BOSS DR12 by Baumann et al. (2019) who found with 95% confidence a non-zero phase shift by free-streaming relics. The parameterization by Baumann et al. (2019), like the standard BAO analysis, involves a semi model-independent parameter β that characterizes the amplitude of the phaseshift and can be transformed into a constraint on N_{eff} , the effective number of neutrino species. The effect of altering N_{eff} in the matter power spectrum, which shifts the phase in the BAOs can be seen in Figure 1. The effect in configuration space can be seen in Figure 2, where the correlation function has been calculated from the power spectrum using the *mcfit* package.² It is apparent from the figures, that the impact of the phase shift from varying N_{eff} on the BAO wiggles is subtle compared to various other impacts N_{eff} has on the power spectrum or correlation function. Nonetheless, it can be detected.

Baumann et al. (2018, 2019) also discuss and provide forecasts for the potential for upcoming galaxy surveys that will probe the Large-scale Structure to constrain the phase shift and N_{eff} . One such survey is the DESI survey (Aghamousa et al. 2016), a 5-year galaxy survey that is currently in progress and began in 2020.³ It is using an instrument that consists of 5000 robot fibres, mounted on the focal plane of the Mayall Telescope at Kitt Peak, Arizona, to measure spectra for 35 million galaxies. The DESI instrument has already detected the BAO signal in their DR1 Data (Adame et al. 2024a) with a 9.1σ level detection at 0.86% precision using a sample of luminous red galaxies (LRGs) and emission line galaxies (ELGs). In Baumann et al. (2018, 2019), it was anticipated using Fisher Matrix Forecasts that DESI will be able to measure the phase shift with an uncertainty of $\sigma(\beta) \sim 0.3$ from their 5-year survey; DESI BAOs + *Planck* may achieve $\sigma(N_{\text{eff}}) = 0.15$, and with the full broadband power spectrum from DESI may achieve $\sigma(N_{\text{eff}}) = 0.087$.

In this paper, we start down this path by constraining the phase shift with DESI DR1 BAO data. Unlike the constraints shown in Baumann et al. (2019), we also extend the methodology to constrain

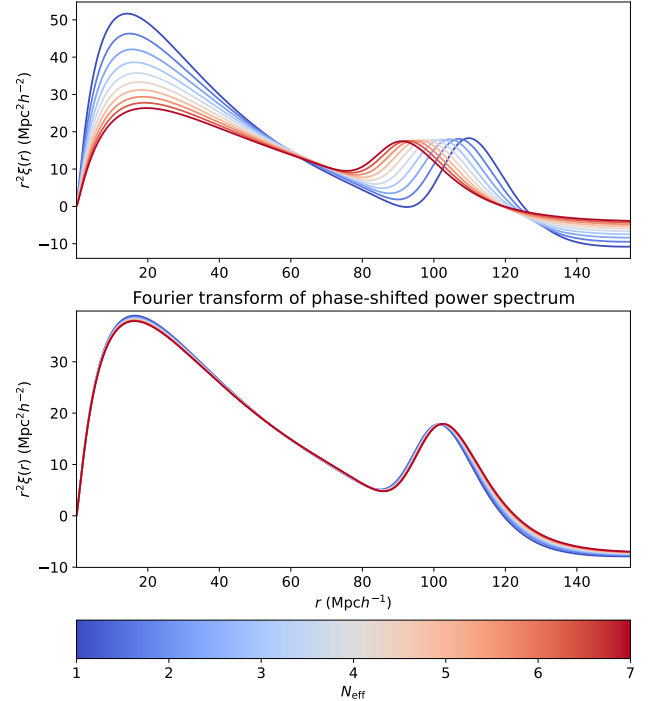


Figure 2. Top panel: the effect of altering N_{eff} on the correlation function, calculated from a Fourier transform of the power spectrum shown in the top panel of Figure 1. Lower panel: the correlation function calculated from the power spectrum, using a Fourier transform, after including a phase shift following the parameterization of the phase shift shown in Baumann et al. (2019). The power spectrum is shifted along the x -axis by shifting the k values by an amount expected by for a given N_{eff} and interpolating the power spectrum. Unlike the top panel, the lower panel shows only the effects due to a phase shift on the correlation function rather than the various impacts that can be seen in the top panel due to N_{eff} , including the phase shift.

β with both the isotropic and anisotropic BAO parameters, α and α_{AP} . In Section 2, we will give an overview of the anisotropic fitting methodology and the parameterization of the phase shift given by Baumann et al. (2019) and our implementation of the method in two BAO fitting codes; *Barry* (Hinton et al. 2020) and *desilike*.⁴ In Section 3, we will show the robustness of the approach and codes applied to mocks produced for the DESI collaboration for datasets including the Bright Galaxy Survey (BGS), LRGs, ELGs and quasars (QSOs), and constraints for the combinations of these datasets. Our results from applying the methodology to the DESI DR1 BAO data will be shown in Section 4 and we conclude in Section 5.

2 METHODOLOGY

In this work we follow the methodology of Baumann et al. (2018, 2019) to constrain the phase shift. As mentioned previously, instead of only constraining the isotropic BAO scaling parameter α and the phase shift, we extend the approach to measure the anisotropic BAO by fitting α_{\parallel} , α_{\perp} and the phase shift amplitude β . Furthermore, we implement this methodology in two codes to fit these parameters; *Barry* and *desilike* which can both fit the BAO wiggles using the galaxy power spectrum or the BAO peak in the correlation function.

² <https://github.com/eelregit/mcfit>

³ <https://www.desi.lbl.gov/>

⁴ <https://desilike.readthedocs.io/en/latest/#>

Having these two approaches will allow us to see the robustness of our constraint under different methodologies.

2.1 Isotropic BAO analysis

In the standard isotropic BAO analysis, the galaxy power spectrum can be split into a smoothed component (or no-wiggle component/broadband component) and a wiggle component,

$$\begin{aligned} P(k) &= P_{\text{nw}}(k) + P_{\text{w}}(k) \\ &= P_{\text{nw}}(k) \left(\frac{P_{\text{w}}(k)}{P_{\text{nw}}(k)} + 1 \right) \\ &= P_{\text{nw}}(k) (O(k) + 1). \end{aligned} \quad (1)$$

The goal of the analysis is to isolate the BAO wiggles from the observed power spectrum, and fit the distortion parameter α which scales the true positions of the BAO peaks and troughs in Fourier space. The distance scaling of the peaks that occurs is by an amount relative to the expected positions of the BAO peaks in a *fiducial* model that is assumed when the observed redshifts of galaxies are transformed to distances, and also relative to a *template* cosmological model that is assumed when one is fitting the BAOs; often these fiducial and template cosmologies are the same. However in general, the parameter α can be defined as

$$\alpha = \frac{D_V(z) r_s^t}{D_V^f(z) r_s}. \quad (2)$$

$D_V(z)$ corresponds to the volume averaged distance,

$$D_V(z) = \left((1+z)^2 D_A^2(z) \frac{cz}{H(z)} \right)^{1/3}, \quad (3)$$

where $H(z)$ is the Hubble parameter at the redshift z corresponding to the redshift of the BAO measurement, and $D_A(z)$ is the angular diameter distance. r_s corresponds to the sound horizon at the baryon drag epoch (at z_d). The quantities with the ‘f’ superscript refer to the expected value in the fiducial model, while those with the ‘t’ superscript refer those in the template model. When all of these models are the same as the true cosmology, $\alpha = 1$; but deviations from unity allow us to quantify the deviation of the models from the true cosmology. α enters the power spectrum as a rescaling of the measured k -modes, and one writes the measured modes $k' = k/\alpha$, where k denotes the true modes. The power spectrum is also scaled by a ratio of the volume averaged distances cubed due to the fact that the rescaling of distances changes the defined survey volume, which must be accounted for as the power spectrum has units of volume. Typically the redshift-space power spectrum $P(k, \mu)$ is decomposed into moments using a Legendre polynomial expansion ($\mathcal{P}_\ell(\mu)$) as

$$P_\ell(k) = \frac{2\ell+1}{2} \int_{-1}^1 d\mu P(k, \mu) \mathcal{P}_\ell(\mu), \quad (4)$$

allowing us to write the following expression for the redshift-space power spectrum as a summation over the power spectrum moments,

$$P(k, \mu) = \sum_\ell P_\ell(k) \mathcal{P}_\ell(\mu). \quad (5)$$

The isotropic analysis allows us to constrain the monopole moment corresponding to $\ell = 0$. Here, $\mu = \cos(\mathbf{k} \cdot \hat{\mathbf{f}})$ – the cosine of the angle between the wavevector of interest and the line-of-sight. The parameter α enters the wiggle power spectrum template as

$$P'_w(k) = P_w^t(k/\alpha). \quad (6)$$

2.2 Anisotropic BAO analysis

In the anisotropic case, it is possible to constrain both the monopole and the quadrupole corresponding to $\ell = 2$. The analysis constrains two distortion parameters, α_{\parallel} that scales the BAO peaks along the line-of-sight while α_{\perp} constrains the BAO peaks transverse to the line-of-sight; when the fiducial cosmology and template cosmology agree with the real cosmology, these parameters are unity. Alternatively, the anisotropic analysis can be parameterized in terms of α defined previously and α_{AP} for the distortions, where α_{AP} is also unity when all three cosmologies are the same. The parameters α_{\parallel} and α_{\perp} are defined as⁵

$$\alpha_{\parallel} = \frac{H^f(z) r_s^t}{H(z) r_s}, \quad (7)$$

$$\alpha_{\perp} = \frac{D_A(z) r_s^t}{D_A^f(z) r_s}. \quad (8)$$

Furthermore, equation 7 and equation 8 can be related to α and α_{AP} as

$$\alpha = \alpha_{\text{iso}} = \alpha_{\parallel}^{1/3} \alpha_{\perp}^{2/3}, \quad (9)$$

$$\alpha_{\text{AP}} = \alpha_{\parallel} / \alpha_{\perp}.$$

If one assumes a flat Λ CDM cosmology, it is possible to directly relate α_{AP} to the matter density Ω_m ,

$$\begin{aligned} \alpha_{\text{AP}} &= \alpha_{\text{AP}}(z, \Omega_m), \\ &= (H(z) D_A(z))^f (H(z, \Omega_m) D_A(z, \Omega_m))^{-1}, \\ &= (E(z) D_A(z) h)^f (E(z, \Omega_m) D_A(z, \Omega_m) h)^{-1}. \end{aligned} \quad (10)$$

where we have used $H(z) = 100 \text{ km s}^{-1} \text{ Mpc}^{-1} h E(z)$. The term containing the angular diameter distance, $D_A(z, \Omega_m) h$, depends on only Ω_m and z . α on the other hand relates to both Ω_m and the comoving sound horizon $r_s h$,

$$\begin{aligned} \alpha &= \alpha(\Omega_m, r_s h), \\ &= \left[\left(\frac{H(z)}{D_A^2(z)} \right)^{1/3} r_s^t \right]^f \left[\left(\frac{H(z)}{D_A^2(z)} \right)^{1/3} r_s \right]^{-1}, \\ &= \left[\left(\frac{E(z)}{D_A^2(z) h^2} \right)^{1/3} r_s^t h \right]^f \left[\left(\frac{E(z)}{D_A^2(z) h^2} \right)^{1/3} r_s h \right]^{-1}. \end{aligned} \quad (11)$$

It is therefore convenient to note that, for a flat Λ CDM cosmology, one can uniquely map from a set of BAO parameters to a cosmological model by first computing Ω_m given α_{AP} , then using this fixed value alongside α to isolate $r_s h$. The distortion parameters enter the wiggle power spectrum template as

$$\begin{aligned} P_w(k, \mu) &= P^t(k(k', \mu'), \mu(k', \mu')), \\ &= P^t(k(\alpha_{\parallel}, \alpha_{\perp}), \mu(\alpha_{\parallel}, \alpha_{\perp})), \end{aligned} \quad (12)$$

where k' and μ' are the observed (distorted) k and μ due to anisotropic distortions. The observed k' , μ' can be related to the

⁵ Strictly, the geometric AP Effect actually is only due to distortions from the ratios $q_{\parallel} = \frac{H^f(z)}{H(z)}$ and $q_{\perp} = \frac{D_A(z)}{D_A^f(z)}$, because the factor of $\frac{r_s^t}{r_s}$ only enters due to the choice of BAO template. However it is common to refer to α_{\parallel} and α_{AP} in the literature when constraining the BAO distortion parameters.

real k , μ as

$$k' = \frac{k}{q_{\perp}} \left[1 + \mu^2 \left(\frac{1}{F^2} - 1 \right) \right]^{1/2}, \quad (13)$$

$$\mu' = \frac{\mu}{F} \left[1 + \mu^2 \left(\frac{1}{F^2} - 1 \right) \right]^{-1/2},$$

where $F = q_{\parallel}/q_{\perp}$, $q_{\parallel} = H^f(z)/H(z)$ and $q_{\perp} = D_A(z)/D_A^f(z)$.

2.3 Anisotropic BAO analysis with β_{ϕ}

Similar to the BAO distortion parameters, the phase shift is constrained by measuring the difference in the amplitude of a phase shift from a template and the true cosmology. However, one should keep in mind that while the phase shift is a parameter similar to α and α_{AP} in that it is model independent and can be transformed into a constraint on cosmology, it is not a geometric distortion but is a physical change to the true k modes in the power spectrum. The BAO wiggle feature can be expressed as a sinusoidal oscillation with a k -dependent amplitude,

$$O_{\text{lin}}(k) \propto A(k) \sin(kr_s + \phi(k)), \quad (14)$$

where ϕ is the phase shift; it is parameterized in [Baumann et al. \(2018, 2019\)](#) as

$$\phi(N_{\text{eff}}, k) = \beta_{\phi}(N_{\text{eff}})f(k). \quad (15)$$

Here β_{ϕ} is the relative amplitude of the phase shift compared to a template model, and $f(k)$ is a fitting function for the scale dependence of the ϕ . When the template cosmology model chosen and the true cosmology match, β_{ϕ} is unity. β_{ϕ} is related to N_{eff} as

$$\beta_{\phi} = \frac{\epsilon_{\nu}}{\epsilon_{\nu}^t} = \frac{N_{\text{eff}}/(N_{\text{eff}} + a_{\nu})}{N_{\text{eff}}^t/(N_{\text{eff}}^t + a_{\nu})}; \quad a_{\nu} = \frac{8}{7} \left(\frac{11}{4} \right)^{4/3}. \quad (16)$$

Given that the phase shift is a physical effect caused by free-streaming relativistic species, rather than an effect that is induced by the choice of the fiducial model used to construct the power spectrum or correlation function, we expect β_{ϕ} to be independent of the choice of fiducial cosmology and only dependent on the template cosmology. If $N_{\text{eff}} = 0$, we also have $\beta_{\phi} = 0$. In the limit $N_{\text{eff}} \rightarrow \infty$, $\beta_{\phi} \approx 2.4$ when $N_{\text{eff}}^t = 3.044$. $f(k)$ is redshift independent and has been approximated by [Baumann et al. \(2018\)](#); it is to first order independent of N_{eff} for a range of values of N_{eff} . This can be seen in Figure 1 of [Baumann et al. \(2019\)](#). The fitting function template $f(k)$ is parameterized as

$$f(k) = \frac{\phi_{\infty}}{1 + (k_*/k)^{\xi}}, \quad (17)$$

with $\phi_{\infty} = 0.227$, $k_* = 0.0324h\text{Mpc}^{-1}$ and $\xi = 0.872$. As $k \rightarrow \infty$, $f(k) \rightarrow \phi_{\infty}$. Finally, the observed wiggle power spectrum can be written in terms of the anisotropic distortion parameters and the phase shift amplitude as

$$P_{\text{w}}(k, \mu) = P^t(k(k', \mu') + (\beta_{\phi} - 1)f(k')/r_s, \mu(k', \mu')), \quad (18)$$

$$= P^t(k(\alpha_{\parallel}, \alpha_{\perp}) + (\beta_{\phi} - 1)f(k')/r_s, \mu(\alpha_{\parallel}, \alpha_{\perp})).$$

It is also possible to directly map the anisotropic BAO distortion parameters to Ω_{m} and $r_s h$ in a flat ΛCDM cosmology. We note here that unlike equation 3.4 in [Baumann et al. \(2019\)](#) we include the impact of the distortions in the scale-dependent function $f(k)$ for the phase shift in equation 18. However, we found there was no impact on the fits to any parameters by choosing to include the distortion k' rather than simply k in $f(k)$ (which is how the model is implemented in *Barry*); however the impact may be more significant in cases one explores exotic models which alter the function $f(k)$.

2.4 Implementation

Our fitting methodology for the BAO scaling parameters and phase shift amplitude has been implemented in both *desilike*⁶ and *Barry*⁷ ([Hinton et al. 2020](#)). These implementations are both *python* packages written for fitting the BAO feature and obtaining constraints on the BAO parameters. While both codes are capable of standard isotropic and anisotropic fits⁸, in this work we have extended *Barry* in order to additionally constrain the phase shift.⁹ *desilike* also contains the implementation via recent updates. While these codes have various available clustering and BAO models to choose from, here we focus on using and implementing the phase shift parameterisation with a model similar to the style of [Beutler et al. \(2017\)](#). This model has been widely used in previous BAO analyses and recently by the DESI collaboration for the analysis of the year 1 data (the model used is presented and discussed in [Chen et al. 2024](#)). We use the same modelling to be consistent with the DESI Year 1 results ([Adame et al. 2024b](#)).

2.4.1 Power spectrum

In *desilike* and *Barry* the redshift-space power spectrum is generically expressed in the following way for the BAO analysis, using the decomposition of the power spectrum into a broadband (no-wiggles) component and a sinusoidal wiggles component as in equation 1 ([Chen et al. 2024](#)),

$$P(k, \mu) = \mathcal{B}(k, \mu)P_{\text{nw}}(k) + C(k, \mu)P_{\text{w}}(k) + \mathcal{D}(k, \mu). \quad (19)$$

\mathcal{B} accounts for peculiar velocity effects such as the Kaiser Effect ([Kaiser 1987](#)) and the Finger-of-God Effect (FOG, [Jackson 1972](#)), C is the propagator which accounts for non-linear evolution of the BAO feature, and \mathcal{D} accounts for additional features in the measured broadband component of the power spectrum not captured by the no-wiggle component, for instance due to systematics or non-linear structure growth. This term is discussed in more detail in sections 2.4.3 and 2.4.4. In our model, we express \mathcal{B} as

$$\mathcal{B}(k, \mu) = (b + f\mu^2)^2 \left[1 + \frac{1}{2}k^2\Sigma_s^2 \right]^{-2} \quad (20)$$

where b represents the linear galaxy bias parameter, f is the growth rate of structure (distinctly different from the fitting function for the neutrino phase shift, $f(k)$), and where both parameters combine to form the Kaiser factor $(b + f\mu^2)^2$. Σ_s accounts for FoG damping, and all three of these are free parameters in the BAO analysis. The propagator is expressed as

$$C = (b + f\mu^2)^2 \exp \left[-\frac{1}{2}k^2(\mu^2\Sigma_{\text{nl},\parallel}^2 + (1 - \mu^2)\Sigma_{\text{nl},\perp}^2) \right] \quad (21)$$

where $\Sigma_{\text{nl},\parallel}$, $\Sigma_{\text{nl},\perp}$ are additional free parameters that account for non-linear damping of the BAO due to bulk motions of galaxies (typically on scales $\sim 10h^{-1}\text{Mpc}$.) separately for damping along and perpendicular to the line-of-sight respectively. For an isotropic analysis this simply reduces to

$$C = (b + f\mu^2)^2 \exp \left[-\frac{1}{2}k^2\Sigma_{\text{nl}}^2 \right], \quad (22)$$

involving only one isotropic damping parameter Σ_{nl} .

⁶ <https://github.com/cosmodesi/desilike>

⁷ <https://barry.readthedocs.io/en/latest/>

⁸ the *Barry* code has been updated since the work presented in [Hinton et al. \(2020\)](#), see more about the improvements in [Chen et al. \(2024\)](#)

⁹ <https://github.com/abbew25/Barry>

2.4.2 Reconstruction

In a BAO analysis it is typical to apply an type of algorithm called *reconstruction* to the data, which enhances the BAO signal allowing for improved signal-to-noise. Data products, such as the power spectrum, where a reconstruction algorithm has been applied are referred to as *post-recon* while those without the application of this algorithm are called *pre-recon*. This algorithm is described in greater detail theoretically in [Chen et al. \(2024\)](#) and practically in [Paillas et al. \(2024\)](#), however the basic steps are described here. First, it involves smoothing the galaxy density field with a Gaussian filter to filter out more non-linear modes. Then, the Zeldovich approximation is used in order to calculate the displacement of the positions of galaxies in space due to structure growth, and this is used to shift the positions of a random catalogue of galaxies and the galaxies in the data by subtracting the calculated linear theory displacement. The reconstructed density field is then given by the difference between the shifted galaxy density field of the data and the shifted random catalogue. The effect of this is to sharpen the BAO feature in the data, because distortions due to non-linear structure growth and the bulk motions of galaxies are largely removed. Consequently, the parameters $\Sigma_{\text{nl},\parallel}$, $\Sigma_{\text{nl},\perp}$ and Σ_s vary between mocks and data that are pre-recon and post-recon, with reconstruction reducing the values of the damping parameters.

In this work we use post-recon mocks that have been reconstructed using the RecSym convention in DESI, in which case the displacement applied to the random catalogue and data are equivalent and the anisotropy in redshift space is preserved (this in contrast to the RecIso formalism – a more detailed discussion of both can also be seen in [Chen et al. 2024](#); [Paillas et al. 2024](#)).

2.4.3 Polynomial broadband methodology

Historically, the term $\mathcal{D}(k, \mu)$ has been modelled using a polynomial expansion. In the methodology of [Beutler et al. \(2017\)](#), this can be expressed for the monopole and quadrupole for the pre-recon data as

$$\mathcal{D}_\ell(k) = \frac{a_{\ell,1}}{k^3} + \frac{a_{\ell,2}}{k^2} + \frac{a_{\ell,3}}{k} + a_{\ell,4} + a_{\ell,5}k. \quad (23)$$

For the post-recon analysis, it is written as

$$\mathcal{D}_\ell(k) = \frac{a_{\ell,1}}{k^3} + \frac{a_{\ell,2}}{k^2} + \frac{a_{\ell,3}}{k} + a_{\ell,4} + a_{\ell,5}k^2. \quad (24)$$

The coefficients $a_{\ell,i}$ and number of polynomial terms are chosen based on the best fit to the data. To be consistent with the DESI methodology and formalism shown in [Chen et al. \(2024\)](#) and [Paillas et al. \(2024\)](#), we fit for all the coefficients in our analysis.

2.4.4 Spline broadband methodology

The polynomial broadband methodology suffers from some limitations (this is described in detail in [Chen et al. 2024](#)) due to the fact it is not always clear what the optimal number or form of polynomial coefficients to use should be, and when transformed to configuration space they may result in a peak (mimicking the BAO peak). Therefore [Chen et al. \(2024\)](#) present a new approach to modelling additional contributions to the broadband power spectrum, using a summation of cubic splines with bases separated by some choice Δ (set to $0.06 h^{-1} \text{Mpc}$ in our work),

$$\mathcal{D}_\ell(k) = \sum_{n=-1}^{\infty} a_{\ell,n} W_3 \left(\frac{k}{\Delta} - n \right). \quad (25)$$

$W_3(k)$ is a fourth order piece-wise cubic spline that is given in

[Chen et al. \(2024\)](#). This approach importantly removes degeneracy between the broadband component of the power spectrum and the BAO peak and reduces the choice of both the form and number of polynomials to a single choice of Δ (which has a well-defined lower bound — it should be larger than half the BAO wavelength). This choice of Δ alongside the range of scales being fit automatically defines the number of free broadband parameters. Distinct terms can also be set for each multipole moment of the power spectrum. In the analysis our choice of fitting scales ($k = 0.02 - 0.30 \text{Mpc}^{-1}h$) and Δ give 7 $a_{\ell,n}$ coefficients to be fit for each multipole. In our analysis, we test the performance of both the spline methodology and the polynomial methodology in our fits to the phase shift.

2.4.5 Correlation function

To analyse the BAO in configuration space, the redshift-space correlation function is simply calculated from a Hankel transform of the redshift-space power spectrum to configuration space. The only difference in our analysis of the correlation function compared to the power spectrum is that we set the number of coefficients to only three for analyses using the polynomial broadband methodology. For the spline broadband methodology, the transformation of the cubic spline basis presented above results in two large scale $n = [0, 1]$ terms for the quadrupole which we include, while the remainder are confined to small scales outside our fitting range ($50 - 150 \text{Mpch}^{-1}$). In addition, the scale-cuts used when fitting the power spectrum to avoid systematics transform into simple polynomials. As such, the final form of $\mathcal{D}_\ell(k)$ for spline-based correlation function fits is completely analogous to that for the power spectrum and takes the form

$$\begin{aligned} \mathcal{D}_0(k) &= a_{0,0} + a_{0,1} \left(\frac{rk_{\min}}{2\pi} \right)^2, \\ \mathcal{D}_2(k) &= a_{0,0} + a_{0,1} \left(\frac{rk_{\min}}{2\pi} \right)^2 + a_{2,0} B_{2,0}(r\Delta) + a_{2,1} B_{2,1}(r\Delta), \end{aligned} \quad (26)$$

where

$$B_{\ell,n}(r\Delta) = i^2 \int \frac{dk k^2}{2\pi^2} W_3 \left(\frac{k}{\Delta} - n \right) j_\ell(kr), \quad (27)$$

is the result of transforming the cubic spline functions and k_{\min} refers to the minimum choice of k used in our Fourier-space fits. $j_\ell(kr)$ are the spherical Bessel functions of the first kind. The reconstruction procedure using RecSym convention is also applied in the case of the correlation function analysis.

3 MOCK VALIDATION

In order to validate the methodology we first apply the fitting procedure in [Barry and desilike](#) to various mocks for the DESI data. The DESI survey strategically splits the survey into dark-time and bright-time components, to optimize detection of galaxies when the moon illuminates the sky (bright-time, so that only bright galaxies at low-redshift can be detected) and dark-time for fainter objects. As such, the DR1 data consists of BGS (galaxies detected under the bright-conditions), LRGs, ELGs and QSOs (see more detail in [Adame et al. 2024b](#)). Mocks are provided for the individual datasets of galaxies detected in the DR1 data set, split into various redshift bins as required, and we obtain fits for each of these individual bins. We also provide combined fits to the mocks by combining the likelihoods for each of the fits to the individual bins. While we produce fits with the β_ϕ parameter using the anisotropic BAO methodology for

Table 1. Summary of DESI DR1 data tracers properties. The LRGs are split across three redshift bins (LRG1, LRG2, LRG3) and ELGs across two (ELG1, ELG2).

Tracer	z	N objects
BGS	0.1 - 0.4	300,017
LRG1	0.4 - 0.6	
LRG2	0.6 - 0.8	2,138,600
LRG3	0.8 - 1.1	
ELG1	0.8 - 1.1	2,432,022
ELG2	1.1 - 1.6	
QSO	0.8 - 2.1	856,652

the majority of the mocks and corresponding data, to be consistent and comparable to the results provided by the DESI Collaboration for the DR1 data (Adame et al. 2024b) we only fit β_ϕ using an isotropic BAO procedure for QSOs, BGS and for ELGs at $z = 0.8 - 1.1$. Furthermore, we fit a combined measurement of the correlation function and power spectrum for ELGs and LRGs at $z = 0.8 - 1.1$ to account for their cross-correlation. Otherwise, following the DESI Collaboration, we neglect cross-correlations between QSOs with ELGs and LRGs from $z = 0.8 - 1.1$ due to the fact that the number of overlapping tracers in the survey volume is likely to be negligible, and neglect cross-correlations between other tracers which are detected in non-overlapping redshift bins. The details of the survey tracers are summarised in the Table 1.

3.1 Fitting DESI first-generation mocks

3.1.1 Description of first-generation mocks

In this paper, DESI first-generation mocks (Adame et al. 2024a,b) refer to a set of single-redshift snapshots of full N-body mocks based on the Abacus Summit simulations (Maksimova et al. 2021).¹⁰ The first-generation mocks are cubic boxes with a *Planck* 2018 (Aghanim et al. 2020) cosmology (called c000 cosmology in this paper, with $N_{\text{eff}} = 3.044$), used here in order to test the BAO fitting methods on mocks with precision far beyond that of DESI DR1. The dark matter haloes are populated in the mocks using a Halo Occupation Distribution algorithm (HOD, Rocher et al. 2023; Yuan et al. 2024). We also make use, where available, of first-generation ‘control variate’ (CV) mocks, which have been processed to reduce the noise in the galaxy clustering signal by subtracting off the intrinsic sample variance in the simulated observables (Hadzhiyska et al. 2023). These allow us to test the methodologies with greater precision, and quantify the effects of systematics when the statistical noise in the mocks is smaller than we expect to see even for the final DESI data. More details about the mocks can also be found in Garcia-Quintero et al. (2024); Mena-Fernandez et al. (2024). The ‘second-generation’ mocks discussed later capture the selection function of the DR1 data and involve an improved HOD algorithm compared to the first-generation mocks. The first-generation mocks do not include systematics in the DESI pipeline like in second-generation mocks. The covariance matrices for the mocks have been produced using 1000 realisations of EZ-mocks (Chuang et al. 2015), which are produced with the same

selection function as is used for the Abacus Summit mocks. We apply the Hartlap correction to the covariance matrices for these mocks (Hartlap et al. 2007; Percival et al. 2014, 2022).

For all the fits to the first-generation mocks, to be consistent with the modelling in Chen et al. (2024), a Gaussian prior $\mathcal{N}(\mu, \sigma)$ with mean μ and width σ has been used for Σ_s given by $\mathcal{N}(2, 2)$ ($\text{Mpc}h^{-1}$), for $\Sigma_{\text{nl},\parallel}$ given by $\mathcal{N}(5, 2)$ ($\text{Mpc}h^{-1}$) and $\Sigma_{\text{nl},\perp}$ given by $\mathcal{N}(2, 1)$ ($\text{Mpc}h^{-1}$). We have allowed β_ϕ to vary over $\mathcal{U}(-1, 3)$ (uniformly over the range $[-1, 3]$) as a minimum range. For polynomial fits, three and five terms with power-law indices of $[-2, -1, 0]$ and $[-1, 0, 1, 2, 3]$ are used to fit the broadband signal for the correlation function and power spectrum respectively. For the spline methodology, seven coefficients are used for the cubic splines and two coefficients are used for the spline basis which is Hankel transformed for the correlation function fits (in addition to two more coefficients for polynomial terms – the details can be seen in Section 2.4.4). We let α vary over $\mathcal{U}(0.8, 1.2)$ (uniformly over the range $[0.8, 1.2]$) and the parameter $\epsilon = \alpha_{\text{AP}}^{1/3} - 1$ varies over $\mathcal{U}(-0.2, 0.2)$ in *Barry* (α_{AP} varies over $\mathcal{U}(-0.2, 0.2)$ in *desilike*).

3.1.2 Comparison of desilike with Baumann et al pipeline

In order to validate the methodology implemented in *desilike* (using the *emcee* sampler, Foreman-Mackey et al. 2013) we begin by fitting the post-recon correlation function of 25 CV ELG mocks at $z = 1.1$ using both this code and the isotropic pipeline of Baumann et al. (2019). The results, which can be seen in Appendix A, indicate the implemented scheme reasonably fits the BAO and phase shift parameters, and we see the expected correlation between α and β_ϕ . We expect that by including α_{AP} as an additional parameter, this should have little impact on the β_ϕ constraints, as there is no degeneracy between these two parameters. The results mainly show there is consistency in the fits to β_ϕ in the isotropic or anisotropic case using the pipeline of Baumann et al. (2016).

3.1.3 Comparison of desilike with Barry

We additionally test the *Barry* fitting code with the CV mocks to validate that the fits are consistent using different fitting tools for the anisotropic fitting pipeline. For all our fits with *Barry* we use the Nautilus nested sampler (Lange 2023). In Figure 3 we show post-recon fits in comparison to fits with *desilike*, where β_ϕ is both fixed or allowed to vary. The difference between the peak of the likelihood for α between the two codes when β_ϕ is free vs when it is fixed is $\sim 0.08\%$, and $\sim 0.03\%$ respectively. The difference in the fit to β_ϕ for the two codes is $\sim 4\%$, with variation occurring along the degeneracy direction for these parameters, although they are consistent within 1σ . In both cases, the differences in α and α_{ap} are well within the expected variance from Chen et al. (2024), and we find no evidence of systematic variation between the two codes.

We also consider the robustness of the fitting methodology in the case the true cosmology of the mocks has N_{eff} set to a value that is not $N_{\text{eff}} = 3.044$, and also in the case the fiducial or template cosmology differs from the cosmology of the mocks. Below we show the result of testing power spectrum mocks with a true underlying cosmology with $N_{\text{eff}} = 3.7$, which we refer to as c003 (‘CV’ mocks were not available for this cosmology however). The fit to the mean of 6 mocks with a c003 cosmology is shown in Figure 4. We use similar priors for Σ_s , $\Sigma_{\text{nl},\parallel}$, $\Sigma_{\text{nl},\perp}$ in these fits. For these mocks an analytic covariance matrix was available (O. Alves et al. 2024).

We can expect when using a template with $N_{\text{eff}} = 3.7$ to fit the

¹⁰ <https://abacussummit.readthedocs.io/en/latest/abacussummit.html>

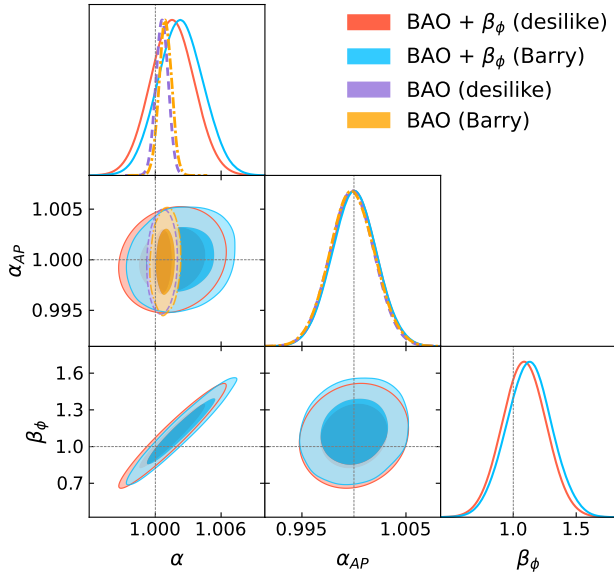


Figure 3. Fits to the mean of 25 CV mocks using *desilike* and *Barry* for the correlation function. Here we show a comparison of the results both when β_ϕ is fixed or allowed to vary freely. The covariance matrix has been reduced by a factor of 25 compared to a single realization.

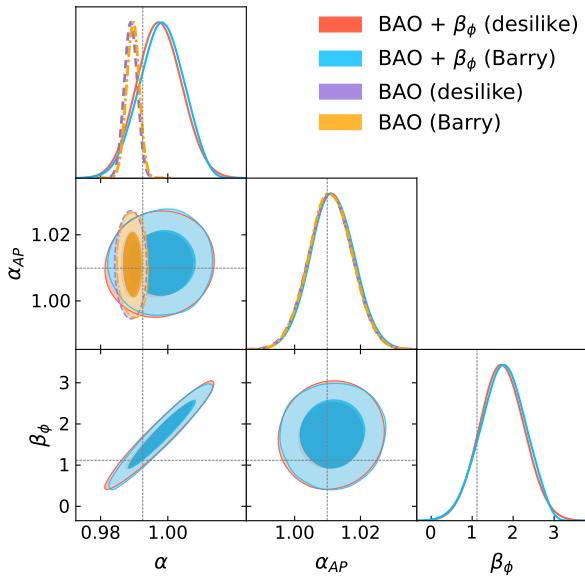


Figure 4. Fits to the mean of 6 power spectrum mocks using *Barry* and *desilike* with the polynomial broadband methodology when the true cosmology of the mocks is $c003$ and the fiducial and template cosmology are set to $c000$. This plot also allows one to compare the robustness of the fits to α when β_ϕ is or is not allowed to vary. The covariance matrix has been reduced by a factor of 6 compared to a single realization.

$c003$ simulations we should recover $\beta_\phi = 1$, but for a template with $N_{\text{eff}} = 3.044$ we expect that $\beta_\phi \approx 1.117$. The fit shown in Figure 4 is statistically consistent with this expectation, although not precise enough to differentiate clearly between the expected value and $\beta_\phi = 1$. However, we still see here that for these mocks there is excellent agreement between the results from our two codes, with no obvious systematic error.

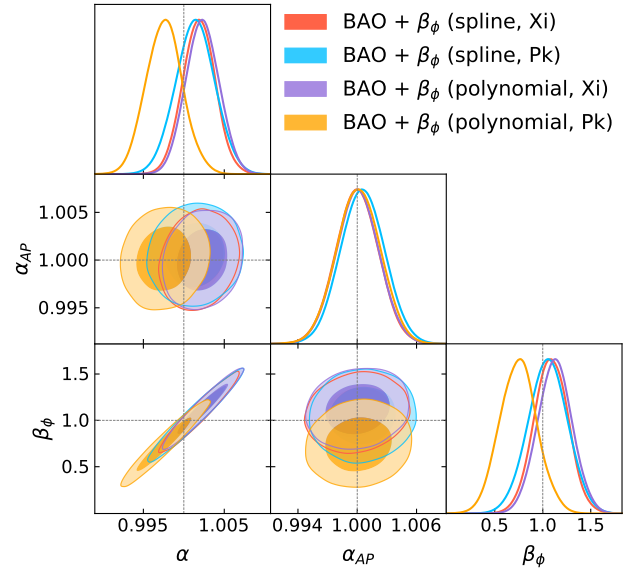


Figure 5. Fits to the mean of 25 CV mocks using *Barry*, comparing spline and polynomial broadband methodologies. The covariance matrix has been reduced by a factor of 25 compared to a single realization.

3.1.4 Robustness of modelling choices in *Barry*

We additionally compare the results of fitting in *Barry* using the polynomial broadband fitting scheme and the spline broadband fitting scheme; these broadband fitting schemes can also be accessed in *desilike*. A comparison of the broadband methodologies for the fit to the mean of 25 post-recon CV power spectrum mocks and CV correlation function mocks ($c000$ cosmology snapshot simulations described earlier) can be seen in Figure 5. A comparison is shown only for fits when the phase shift is allowed to vary; for fits where the phase shift is fixed (standard BAO analysis) we do not see any significant difference in the fits using either broadband methodology or choice of clustering statistic (this can be seen in Appendix B). However, as can be appreciated from Figure 5 there is a noticeable difference in the fits to α and β_ϕ between the two different broadband methodologies for the power spectrum, although the variation to the parameters lies along their degeneracy direction and the fits are consistent with the truth within 1σ .

In Table 2 we show the average difference between the fits to 25 mocks and the difference between the fits to the mocks means for β_ϕ when using the two choices of broadband fitting methodologies, for all the different cases discussed here. Considering the full set of measurements, the polynomial method applied to the power spectrum appears to be the outlier; we find a systematic difference in the fit to β_ϕ with a significance of 3σ compared to results from the pipeline using the polynomial method with the correlation function or instead using the spline broadband fitting method with either the power spectrum or correlation function. We find no other significant shifts in the fit to β_ϕ under other comparisons between variations to the pipeline. As such, we treat the correlation function as our default going forward, interchanging between spline and polynomial broadband for various tests as these demonstrate excellent consistency. As such, we do not adopt any systematic error associated with this choice, although caution that this difference should be investigated further for future DESI data releases where we expect tighter constraints. Nonetheless, we note that (given we are fitting the average of 25 mocks) the size of this shift in β_ϕ (shown in Table 2) is much

Table 2. The difference in the best fit to β_ϕ , when different broadband methodologies are used. Here we compare the difference in the best fit to the mean of 25 mocks, \bar{P}_w , vs the mean of separate best fits to 25 mocks for the ELGs at $z = 1.1$ after reconstruction. The brackets show the significance of the difference in units of σ (where we use the error on the mean as the uncertainty).

Mock data	$ \langle \beta_{\phi, \text{poly}} - \beta_{\phi, \text{spline}} \rangle _{\bar{P}_w}$ Mock mean	$\frac{1}{25} \sum_i^{25} \beta_{\phi, \text{poly}} - \beta_{\phi, \text{spline}} _i$ 25 mocks
Pk	0.40 (2.00)	0.35 (1.75)
Pk CV	0.30 (2.40)	0.29 (2.32)
Xi	0.09 (0.45)	0.08 (0.40)
Xi CV	0.04 (0.32)	0.05 (0.40)

Table 3. A comparison of the absolute difference to the best fits to the BAO and phase shift parameters for the mean of the CV mocks, \bar{P}_w , for ELGs at $z = 1.1$, when the fitting pipeline is varied. The estimate of the significance of the difference relative to the error on the mean is given in the brackets for β_ϕ .

Comparison	$100\Delta\alpha _{\bar{P}_w}$	$\Delta 100\alpha_{\text{AP}} _{\bar{P}_w}$	$\Delta\beta_\phi _{\bar{P}_w}$
<i>Barry vs desilike</i>			
(Xi, CV, polynomial)	0.08 (0.53)	0.000 (0.00)	0.04 (0.32)
Pk vs Xi			
(Barry, CV, polynomial)	0.47 (3.13)	0.010 (0.01)	0.38 (3.04)
Pk vs Xi			
(Barry, CV, spline)	0.05 (0.33)	0.070 (0.05)	0.04 (0.32)
Spline vs polynomial			
(Barry, CV, Pk)	0.38 (2.53)	0.040 (0.02)	0.30 (1.71)
Spline vs polynomial			
(Barry, CV, Xi)	0.04 (0.05)	0.001 (1.43)	0.04 (0.32)
c000 vs c003 fiducial			
(Barry, Pk, polynomial)	–	–	0.18 (1.9)

smaller than we expect for the DESI DR1 or second-generation mock precision, and there is no clear evidence that this shift is systematic rather than statistical (given the fit still overlaps with the truth at 1σ). As shown later, we also find our results for the second-generation mocks and DR1 data are robust to changes in the broadband methodology.

The effect of altering the number of free terms used in the fitting the polynomial broadband terms, the prior ranges used for the nuisance parameters, the choice of the effective redshift for the BAO template or the Boltzmann-solver used to generate the template at a fixed cosmology (which used a *Planck* 2018 cosmology with $z = 0.0$, [Aghanim et al. 2020](#)) and the choice of k_{min} used had little effect on the fits. It should be noted that there can be an impact on the best choice of priors used for nuisance parameters *if* the effective redshift of the BAO template is altered significantly, because some of the nuisance parameters are redshift dependent. However, the optimal choice of priors was thoroughly tested in [Chen et al. \(2024\)](#) and we used these results to inform our choices of priors used for the fits to the mocks. To test the methodology thoroughly, we investigated the effect of altering the method used to smooth the power spectrum to isolate the wobble component of the power spectrum $P_w(k)$ from the no-wobble component $P_{\text{nw}}(k)$. In *Barry* there are currently three methods that can be specified to smooth the power spectrum to isolate these, however it was also found to make negligible difference to the fits of the mocks. In Table 3 we summarise the most significant differences in the fits to α , α_{AP} and β_ϕ for different modelling choices

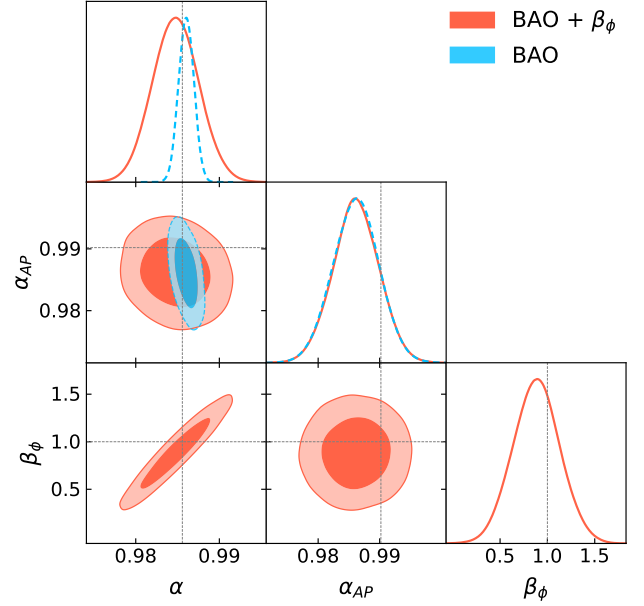


Figure 6. Similar to Figure 4, however only showing the fit to the mean of 25 CV mocks with the polynomial broadband methodology in the case where the template and true cosmology are both set to c000, while the fiducial cosmology is set to c003. In this case, we still expect to recover $\beta_\phi = 1.0$. These fits demonstrate that our method is robust to the choice of fiducial cosmology.

that we identified. The most significant systematic is the difference we see in the fits for the power spectrum compared to the correlation function in the case we apply fits using the polynomial broadband scheme, which further supports our choice to treat the spline-based method as our default.

It is interesting to test whether we still recover $\beta_\phi = 1$ in the case we alter the fiducial cosmology. This is because in the case the template is set to have $N_{\text{eff}} = 3.044$ such that it is the same as the true cosmology, we expect $\beta_\phi = 1$, regardless of the choice of fiducial cosmology for the clustering (this does not apply for α and α_{AP} , whose truth depends on both the true, fiducial and template cosmology). As mentioned earlier, this is because changing N_{eff} (and thus β_ϕ) in the fiducial cosmology should not alter the fit to β_ϕ since β_ϕ arises as a physical shifting of the k modes in the BAO wiggles rather than a geometric distortion (AP Effect) that arises from transforming between redshift-space and real-space co-ordinates. To test this, we fit the mean of the 25 mocks (non CV mocks) again in Figure 6. We use c000 mocks (for the truth and template) where the fiducial cosmology is set to the c003. For brevity we show only the results using the polynomial broadband methodology and we show the absolute difference in the fit to β_ϕ in this scenario in Table 3. Note this *differs* from Figure 4, because here we have altered the fiducial cosmology rather than the real cosmology. The effect of the fiducial (grid) cosmology in DESI mocks for the standard BAO analysis is studied in detail in [Pérez-Fernández et al. \(2024\)](#) for the more sophisticated ‘second-generation’ mocks.

3.1.5 Summary

Overall, our results show a clear degeneracy between α and β_ϕ , which indicates it may be important to include β_ϕ as a free parameter when fitting the BAOs generally (although as we will show later,

applying an informative prior to this recovers the published DESI Year 1 results (Adame et al. 2024a). Of course, when comparing the systematic differences to the fits in α for the standard case vs the case where we include β_ϕ , the impact is insignificant, due to the fact β_ϕ is weakly constrained. However, for future data we may expect it to be possible the degeneracy between α and β_ϕ could lead to small systematic biases in the case β_ϕ is fixed to one but the data prefers a different value.

From Table 3 and Figure 5, it is apparent that the fits using the polynomial broadband method for the power spectrum data results in a difference between polynomial and spline fitting methodologies at a significance of 3σ ; for fits where β_ϕ is a free parameter, $\sigma_{\text{sys}}(\beta_\phi) = \pm 0.38$. Given we find no other methodologies result in such systematics, we avoid using the polynomial fitting method for power spectrum fits for the second-generation mocks and data. As mentioned previously, we find all other choices explored for the fitting methodology do not show significant evidence of systematic differences between the best fits to the BAO parameters or β_ϕ relative to the statistical uncertainty in the fits, although we caution this will need to be considered carefully for future DESI data releases.

3.2 Fitting DESI second-generation mocks with *desilike*

In this section we show the results of fitting realistic second-generation mocks. Unlike the first-generation mocks, these include potential data systematics and selection functions matching the DESI data (Adame et al. 2024a,b). We explore fits in which we do not reduce the covariance on the mocks in order to see the expected constraining power for β_ϕ with the realistic uncertainty for a single realisation. For these fits, the covariance matrices for the correlation function are semi-analytic and are created using *RascalC* (Philcox et al. 2020; Rashkovetskyi et al. 2024),¹¹ while for the power spectrum the covariances are made using *covaPT* (Wadekar & Scoccimarro 2020; O. Alves et al. 2024).¹²

3.2.1 Fits to β_ϕ from individual tracers

Figure 7 shows fits to the individual mocks for the correlation function of each tracer produced using *desilike* and *Barry*; we show fits with the post-recon mocks. We only show the fits using the spline broadband methodology. As with the real data results in section 4, our ‘baseline’ results will use the ‘spline’ methodology to be consistent with Adame et al. (2024b,a). However, we expect based on the analysis of systematics from first-generation mocks presented earlier, the second-generation fits will be independent of the choice between a spline or polynomial broadband approach as they are consistent when using the correlation function. For ELG1 and LRG3 which overlap in redshift, we use a combined mock for the correlation function (the same is used for the fits to the real data). The priors we use on nuisance parameters for second-generation mocks are specified in Table 5. For polynomial fits we set the coefficients for the powers in the fit the broadband shape as $[-2, -1, 0]$ and $[-1, 0, 1, 2, 3]$ for the correlation function and power spectrum respectively. Seven coefficients are used to fit the broadband shape using the spline methodology for power spectrum fits (and as before, the Hankel transformation of the cubic splines to configuration space results in fitting just two coefficients, in addition to two more coefficients for polynomial terms).

¹¹ <https://github.com/misharash/RascalC-scripts/tree/DESI2024/DESI/Y1>

¹² <https://github.com/cosmodesi/thecov>

It is clear that there is consistency in the fits between *Barry* and *desilike* tracers. The only significant differences are for fits in cases where neither *Barry* or *desilike* obtains a strong constraint on the BAO parameters and β_ϕ . In such cases, β_ϕ can hit the end range of the priors used, and we may expect some differences due to differences in how the sampling is performed or due to, subtle differences in the modelling of the Kaiser factor between *desilike* and *Barry* (see discussion in Adame et al. 2024a, although it is expected that these model differences will have negligible effect on the fits to the BAO parameters and β_ϕ and only affect the fits to the nuisance parameters involving the galaxy bias). For the more constraining tracers (i.e., LRG3+ELG1), we see excellent agreement between the codes and both *Barry* and *desilike* obtain unbiased constraints on the phase shift, which validates our methodology for application to the DR1 data. Table 4 shows the difference (on average) between the fit to each BAO parameter + β_ϕ between *Barry* and *desilike*, and for comparison the difference between the fit to the mock means. This, like previously for the first-generation mocks, allows us to verify any potential systematic uncertainties on the fits to the parameters due to differences between the fitting codes, which can be considered in the error budget for the fits to the data. However, for each of the tracers, the relative difference in the fits to each parameter to the statistical uncertainty on the mean is $\lesssim 2.1\sigma$ for α , $\lesssim 2.6\sigma$ for β_ϕ and $\lesssim 0.5\sigma$ for α_{AP} ; the more weakly constraining tracers tend to show larger differences. This indicates no strong detections of any systematic differences between the codes, and that any systematics are far below the expected precision of the Year 1 data (noting that the statistical error on the data is expected to be 5 times larger than the error on the mean used here).

3.2.2 Determining a combined fit to β_ϕ from multiple tracers

We are also interested in looking at the combined constraining power for β_ϕ from the tracers in addition to the constraints from individual tracers. In order to do this, we take a mock for each tracer, then importance sample the individual constraints LRG1, LRG2 and ELG2 to weight the fit to β_ϕ for the tracer that obtains the most constraining fits, LRG3+ELG1. In this process, we are effectively computing the posterior distribution of β_ϕ from a combined fit of LRG1, LRG2, LRG3+ELG1 and ELG2,

$$P_{\text{combined}}(\beta_\phi) \propto \prod_i \int d\alpha_i d\alpha_{\text{AP},i} P_i(\alpha_i, \alpha_{\text{AP},i}, \beta_\phi | \xi_i), \quad (28)$$

where the index i runs over LRG1, LRG2, LRG3+ELG1 and ELG2 and the individual α and α_{AP} constraints are treated as independent, while β_ϕ is shared. Given that BGS and QSOs obtain weak constraints on β_ϕ , we only use LRGs and ELGs for the combined fits to the mocks and data. This result, which we will refer to as ‘combined fits’ to the mocks can be seen in Figure 8. This shows we can obtain reasonable fits to β_ϕ using this methodology and find that combining the multiple tracers improves the uncertainty on β_ϕ by a factor ~ 1.9 compared to the fits to LRG3+ELG1 alone. The fits are also consistent between *Barry* and *desilike* when combining the tracers in this way. The fits here are done using individual mock fits with the ‘baseline’ methodology. The average absolute difference of each mock fit to the combination of the tracers, for fits to the tracers done using *desilike* and *Barry* is $\Delta\beta_\phi = 0.431$ (or $\frac{\Delta}{\sigma} = 1.282$ where σ is the weighted standard error of the mean of the combined fits). The absolute difference between the fits to the mock mean data (average correlation function of 25 mocks) is $\Delta\beta_\phi = 0.809$.

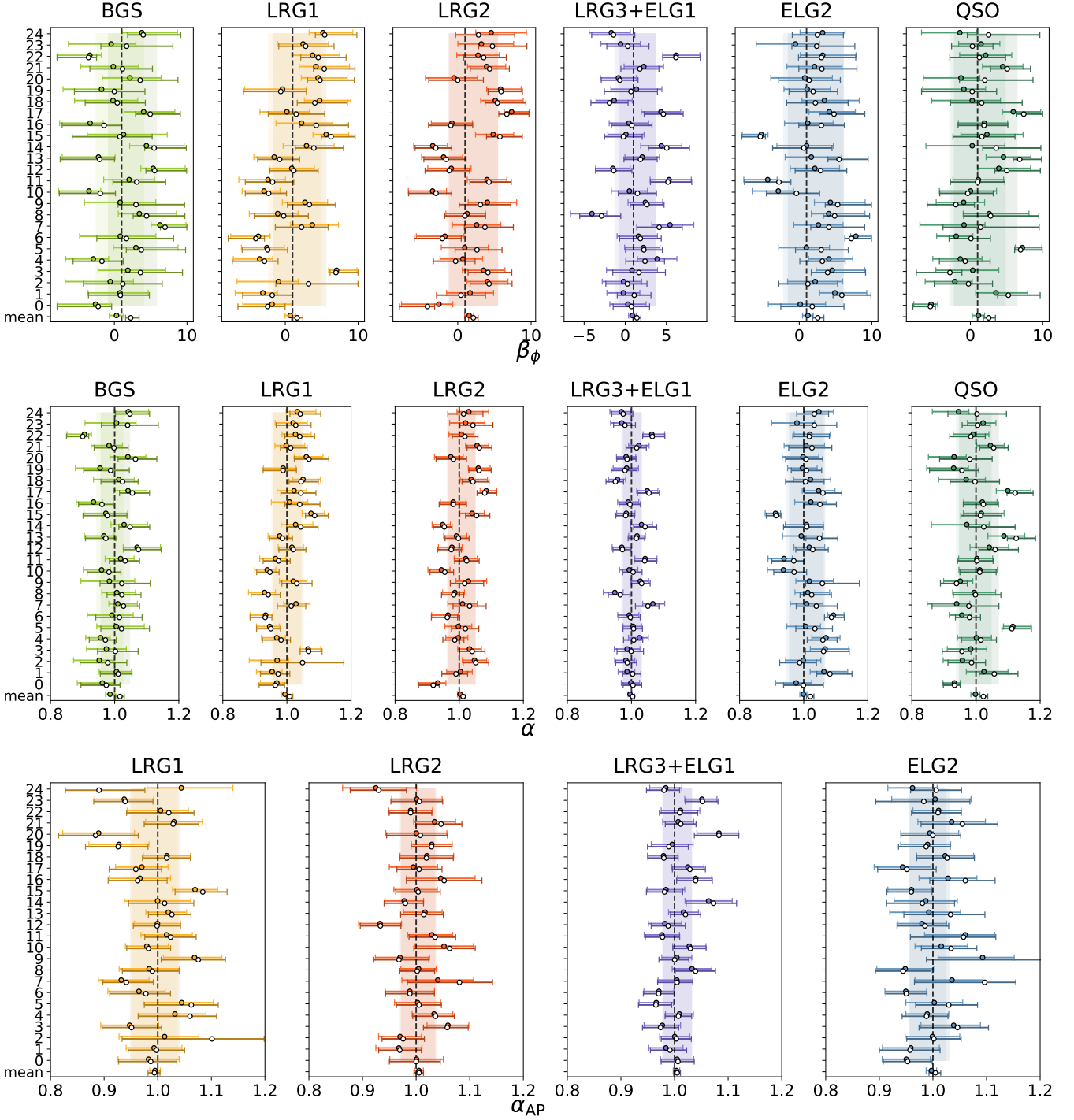


Figure 7. Our fits of the 25 mocks and the mean for β_ϕ (top panel), α (middle panel) and α_{AP} (lower panel), for the 6 DESI samples considered here. The coloured points show *desilike* fits while the white points show the fits using *Barry*. Shaded regions show one standard deviation about the mean fit for the 25 mocks, where the darker colored shaded regions are *desilike* and the lighter are *Barry*. The mean and standard deviation has been weighted by the uncertainty on each mock, so that more poorly constrained fits have less weight in the mean. For the BGS and QSO samples, we only fit an isotropic BAO model, and hence do not report α_{AP} .

4 RESULTS WITH DR1 DESI DATA

Having studied the robustness of our fitting methodology to different BAO fitting software and analysis choices in the previous section, we present fits to the BAO parameters and phase shift β_ϕ with the DR1 data. In all cases, we use the same choices of coefficients for

the broadband fitting and choices of priors as done for our fits to second-generation mocks. These choices are the same as those used for the BAO results presented by [Adame et al. \(2024b,a\)](#). For the remainder of this paper, unless stated otherwise, we will refer to and present our main results using the ‘baseline’ methodology; as before,

Table 4. Average of the difference in the fits to α , α_{AP} and β_ϕ between *Barry* and *desilike*. The numbers in brackets also give this uncertainty in the number of standard deviations (taking the weighted standard deviation of the 25 mocks) - thus quantifying the significance of the difference in numbers of σ . We also show for comparison the difference between the fits to the mock means, \bar{P}_w , for each parameter.

Tracer	Δx from the weighted mean of 25 mocks, $\frac{1}{25} \sum_i^{25} x_{\text{Barry}} - x_{\text{desilike}} \left(\frac{\Delta x}{\sigma}\right)$			Δ from fit to data mock mean \bar{P}_w		
	$100\Delta\alpha$	$100\Delta\alpha_{\text{AP}}$	$\Delta\beta_\phi$	$100\Delta\alpha _{\bar{P}_w}$	$100\Delta\alpha_{\text{AP}} _{\bar{P}_w}$	$\Delta\beta_\phi _{\bar{P}_w}$
BGS	1.7 (2.1)	–	1.711 (2.62)	0.03	–	1.950
LRG1	0.7 (0.8)	< 0.1 (< 0.1)	0.570 (0.80)	1.5	0.1	0.947
LRG2	0.2 (0.2)	< 0.1 (< 0.1)	0.550 (0.82)	0.9	< 0.1	0.570
LRG3+ELG1	0.3 (0.5)	< 0.1 (< 0.1)	0.239 (0.49)	0.8	0.1	0.550
ELG2	0.7 (0.6)	0.3 (0.5)	0.361 (0.44)	2.2	0.7	1.361
QSO	1.6 (1.5)	–	1.13 (1.47)	2.5	–	1.425

Table 5. Summary of the choices of priors and ranges used for fitting the second-generation mocks and DR1 data for each DESI tracer. The subscript i denotes different tracer bins (BGS, LRG1, LRG2 etc.) and thus allows us to specify cases where the prior differs for specific cases which are otherwise the same.

Parameter	Gaussian prior: $\mathcal{N}(\mu, \sigma)$		
	Post-recon	Pre-recon	
Σ_S ($\text{Mpc}h^{-1}$)	$\mathcal{N}(2, 2)$	$\mathcal{N}(2, 2)$	
$\Sigma_{\text{nl},\parallel}$ ($\text{Mpc}h^{-1}$)	$\mathcal{N}(6, 2)$	$\mathcal{N}(x_i, 2)$	$x_{\text{ELG2}} = 8.5$ else $x_i = 9$
Σ_{nl} ($\text{Mpc}h^{-1}$)	$\mathcal{N}(x_i, 2)$	$\mathcal{N}(y_i, 2)$	$x_{\text{BGS}} = 8,$ $x_{\text{QSO}} = 6,$ $y_{\text{BGS}} = 10,$ $y_{\text{QSO}} = 9$
$\Sigma_{\text{nl},\perp}$ ($\text{Mpc}h^{-1}$)	$\mathcal{N}(3, 1)$	$\mathcal{N}(x_i, 1)$	$x_{\text{BGS}} = 6.5,$ $x_{\text{QSO}} = 3.5$ else $x_i = 4.5$
b	$\mathcal{U}(0.5, 4)$	$\mathcal{U}(0.5, 4)$	
β_ϕ	$\mathcal{U}(-8, 10)$	$\mathcal{U}(-8, 10)$	
α	$\mathcal{U}(0.8, 1.2)$	$\mathcal{U}(0.8, 1.2)$	
$\epsilon = (\alpha_{\text{AP}}^{1/3} - 1)$ (<i>Barry</i>)	$\mathcal{U}(-0.2, 0.2)$	$\mathcal{U}(-0.2, 0.2)$	
α_{AP} (<i>desilike</i>)	$\mathcal{U}(0.8, 1.2)$	$\mathcal{U}(0.8, 1.2)$	

the ‘baseline’ fits involve post-recon fits to the correlation function using the spline fitting methodology and using the *desilike* software.

Constraints from individual tracers

In Figure 9 we show the individual fits to the BAO distortion parameters α_{\parallel} and α_{\perp} and phase shift β_ϕ for tracers for the DR1 data. The figure also allows a comparison of the baseline results to various individual changes to the fitting pipeline, allowing one to see how robust our results are. One can see how the best fits vary for each tracer under various choices;

- when we do not apply reconstruction to the data,
- when we use the polynomial broadband fitting methodology rather than the spline approach,
- when we fit the power spectrum rather than the correlation function,
- or when we produce the fits with *Barry* rather than *desilike*.

Compared to the fits presented in Adame et al. (2024a) for DESI DR1 (see Figure 12 in their work which is analogous to our Figure 9), there is slightly less consistency in our fits presented when the pipeline is varied; the results shown in Adame et al. (2024a) are more statistically robust to changes. This is most noticeable (and expected) for the pre-recon fits, due to the fact that not applying reconstruction significantly

weakens the constraints. However, we can expect that for all of the fits, the strong degeneracy between α and β_ϕ should lead to less constraints that move along this degeneracy direction due to statistical noise. We also do not expect very strong constraints from BGS or QSO tracers given the results with the mocks showed that these tracers are much less constraining when β_ϕ is allowed to vary, and this is apparent in our results.

It is also important to validate that our fits to α and α_{AP} are consistent with those of the DESI DR1 results presented in Adame et al. (2024b,a) and that the additional uncertainty in our fits when β_ϕ is allowed to vary does not indicate that the uncertainty in the DESI DR1 results are underestimated. To check this, we recalculated these parameters in a thin slice of the parameter space for β_ϕ by importance sampling the data to impose a prior. This was done by taking the *Planck* 2018 MCMC chain for N_{eff} from fits to the $\Lambda\text{CDM} + N_{\text{eff}}$ model, which gives $N_{\text{eff}} = 2.99 \pm 0.17$. In principle, we expect that this is equivalent to rerunning the fits with a very tight informative prior on β_ϕ from *Planck*. In doing so, we found the best fits to the parameters expressed as α and α_{AP} were fully consistent with the DR1 results presented in Adame et al. (2024a). The fits and comparison to the numbers in Adame et al. (2024a) can be seen in Table 6. The 1σ uncertainty on α_{\parallel} varies by approximately 5 – 8% for different tracers, and for α_{\perp} there is a 3 – 15% variation in the 1σ uncertainty. We additionally looked at the constraints in the case when the width of the *Planck* prior for N_{eff} was increased by a factor of 10 times; the fits are still consistent with those presented in Adame et al. (2024a) and only the fits to β_ϕ are weakened.

We also show the correlation function data and best fit models for each tracer for our baseline fits in Figure 10. Unlike the results presented in Adame et al. (2024a), the model here shows the fit to the data when β_ϕ is included in the analysis. For comparison, Figures 5 and 7 in Adame et al. (2024a) show the model fits compared to the data for the standard BAO analysis. The χ^2 goodness-of-fit and number of degrees of freedom of each tracer is given in Table 7 and in all cases these are comparable to those presented in Table 15 of Adame et al. (2024a) and demonstrate excellent fits.

Figure 11 shows the individual fits to each tracer and the posterior distributions for our parameters of interest. The triangle plot on the left allows one to see the posterior distribution for each tracer for α , α_{AP} (excluding BGS and QSOs) and β_ϕ . Each individual bin for the tracers gives relatively consistent fits on β_ϕ (we do not expect consistency for the α , α_{AP} as they are redshift dependent). The BGS and QSO constraints show the largest differences, but as mentioned previously, this is likely because QSOs and the BGS data individually are not able to constrain the β_ϕ parameter in addition to α strongly. Assuming a flat ΛCDM cosmological model, the anisotropic BAO constraints can also be uniquely mapped to a constraint on Ω_m and $r_s h$ (see equation 10 and equation 11). These are shown in the right-

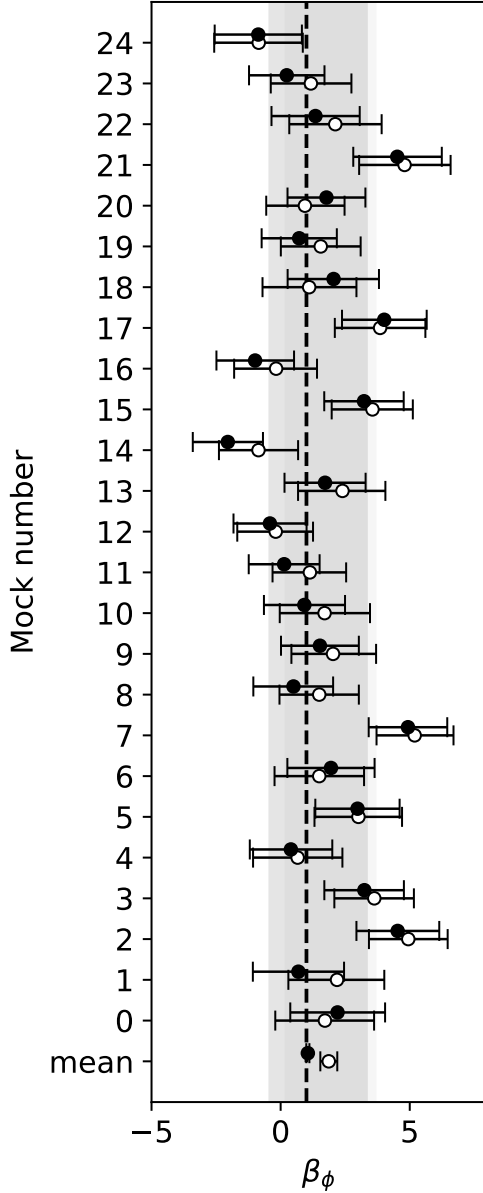


Figure 8. Our fits to β_ϕ from the combinations of the LRGs and ELGs (all tracer bins except QSOs and BGS) with the second-generation mocks, for *desilike* (black points) and *Barry* (white points). The shaded regions show the (weighted) 1-standard deviation about the weighted mean for the fits to individual mocks, the fit to the mean of the mocks is shown at the bottom of the plot.

hand panel of Figure 11. As is shown in the DESI DR1 results in Figure 2 of Adame et al. (2024b), the contours for $r_s h$ and Ω_m have a rotating degeneracy direction for different tracers (due to the changing redshift of each tracer bin), but the constraints between different tracers are internally consistent and the combination allows for a tighter constraint on all parameters.

4.1 Combined constraints and cosmological interpretation

As our different tracers give consistent cosmological results, we can combine them using the methodology described in section 3.2.2 to

Table 6. Constraints on β_ϕ , α and α_{AP} from the DR1 data baseline results. We also include the case where a tight prior is included on β_ϕ by importance sampling with the *Planck* 2018 Λ CDM + N_{eff} MCMC chain. Results quoted from Adame et al. (2024a) are also presented for comparison, demonstrating excellent agreement between our work at previous DESI results when an informative prior on β_ϕ is included.

Data	β_ϕ	α	α_{AP}
<i>(β_ϕ free)</i>			
BGS	$-0.1^{+4.2}_{-5.0}$	$0.971^{+0.05}_{-0.066}$	–
LRG1	3.7 ± 3.2	1.014 ± 0.044	0.915 ± 0.043
LRG2	1.9 ± 4.2	0.979 ± 0.057	1.048 ± 0.048
LRG3+ELG1	2.1 ± 2.6	$1.012^{+0.031}_{-0.035}$	1.028 ± 0.030
ELG2	$3.0^{+3.6}_{-3.2}$	1.018 ± 0.052	0.986 ± 0.045
QSO	$5.9^{+4.0}_{-2.3}$	$1.087^{+0.073}_{-0.045}$	–
<i>(β_ϕ free + Planck prior on N_{eff})</i>			
BGS	0.97 ± 0.04	0.982 ± 0.020	–
LRG1	0.97 ± 0.04	0.979 ± 0.012	0.915 ± 0.041
LRG2	0.98 ± 0.04	0.966 ± 0.013	$1.047^{+0.047}_{-0.052}$
LRG3+ELG1	0.97 ± 0.04	0.998 ± 0.008	1.026 ± 0.029
ELG2	0.97 ± 0.04	0.987 ± 0.015	0.988 ± 0.043
QSO	0.98 ± 0.04	0.998 ± 0.024	–
<i>(Results presented in Adame et al. 2024a)</i>			
BGS	–	0.983 ± 0.019	–
LRG1	–	0.979 ± 0.011	0.915 ± 0.037
LRG2	–	0.966 ± 0.012	1.046 ± 0.043
LRG3+ELG1	–	0.998 ± 0.008	1.026 ± 0.028
ELG2	–	0.988 ± 0.015	0.990 ± 0.047
QSO	–	1.002 ± 0.026	–

Table 7. The χ^2 and degrees-of-freedom (dof) for each of the Baseline fits to the different DESI tracers when β_ϕ is allowed to vary (corresponding to the data shown in Figure 10).

Tracer	χ^2/dof
BGS	15.8/14
LRG1	40.8/36
LRG2	40.6/36
LRG3+ELG1	31.6/36
ELG2	59.8/36
QSO	28.8/14

combine the ELG and LRG mocks. The left panel of Figure 12 focuses on just the 1-dimensional posterior for β_ϕ and includes the result for the combined fit to the tracers as a black-dashed line. The right panel of Figure 12 shows the contours for the combined fits for Ω_m and $r_s h$ when a flat Λ CDM model has been assumed.

Additionally, we show various results when a prior on α and α_{AP} from *Planck* is included (following the approach used by Baumann et al. 2019) by importance sampling the fits to each tracer with the information from the *Planck* 2018 MCMC chains for TT+TE+EE+

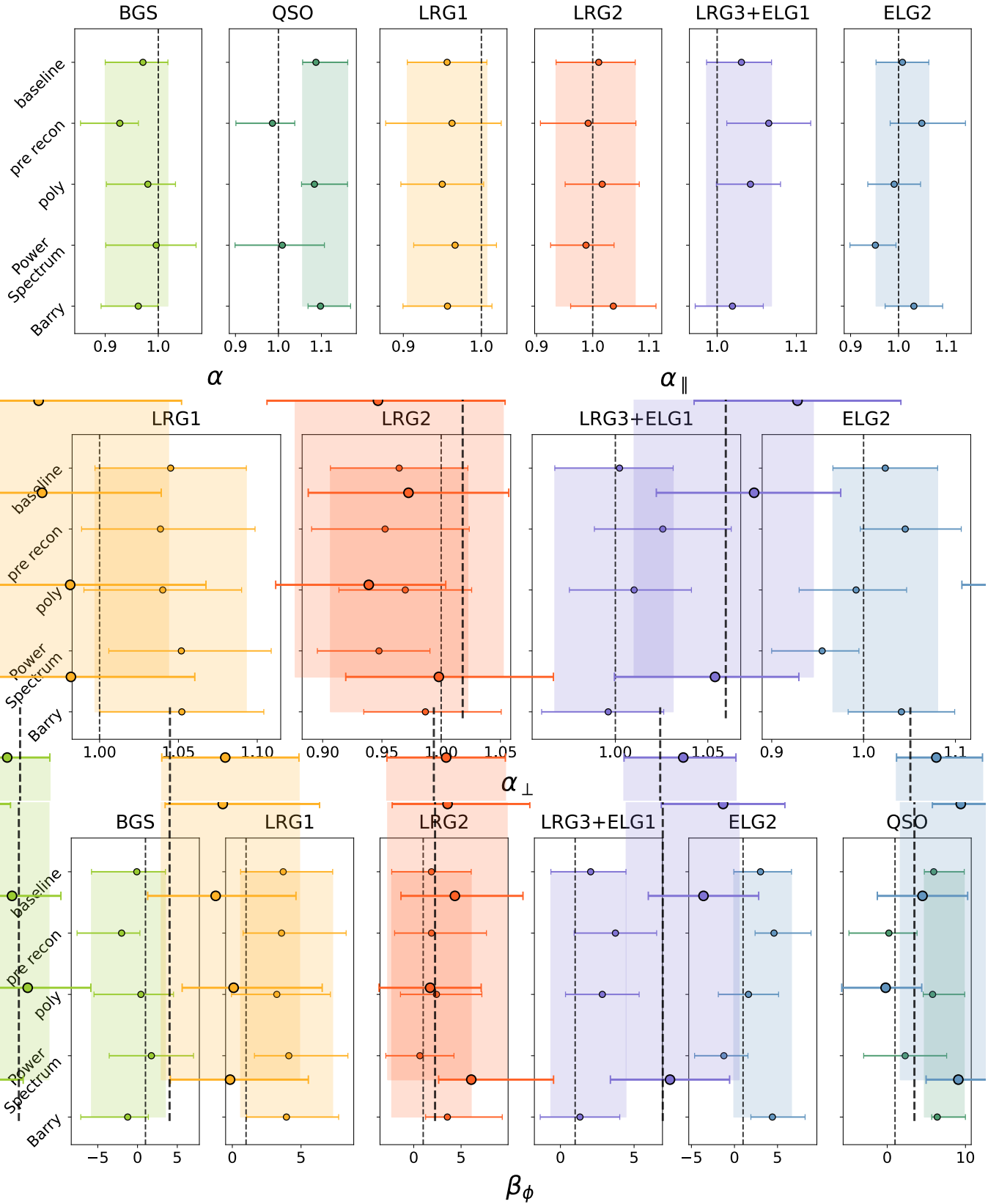


Figure 9. Our fits to the DESI tracers in DR1. For ease of interpretation for the distortions to physical distances, we plot α_{\parallel} , α_{\perp} in place of α and α_{AP} and additionally β_{ϕ} . For BGS and QSOs we only study the isotropic scaling; as such we only plot α .

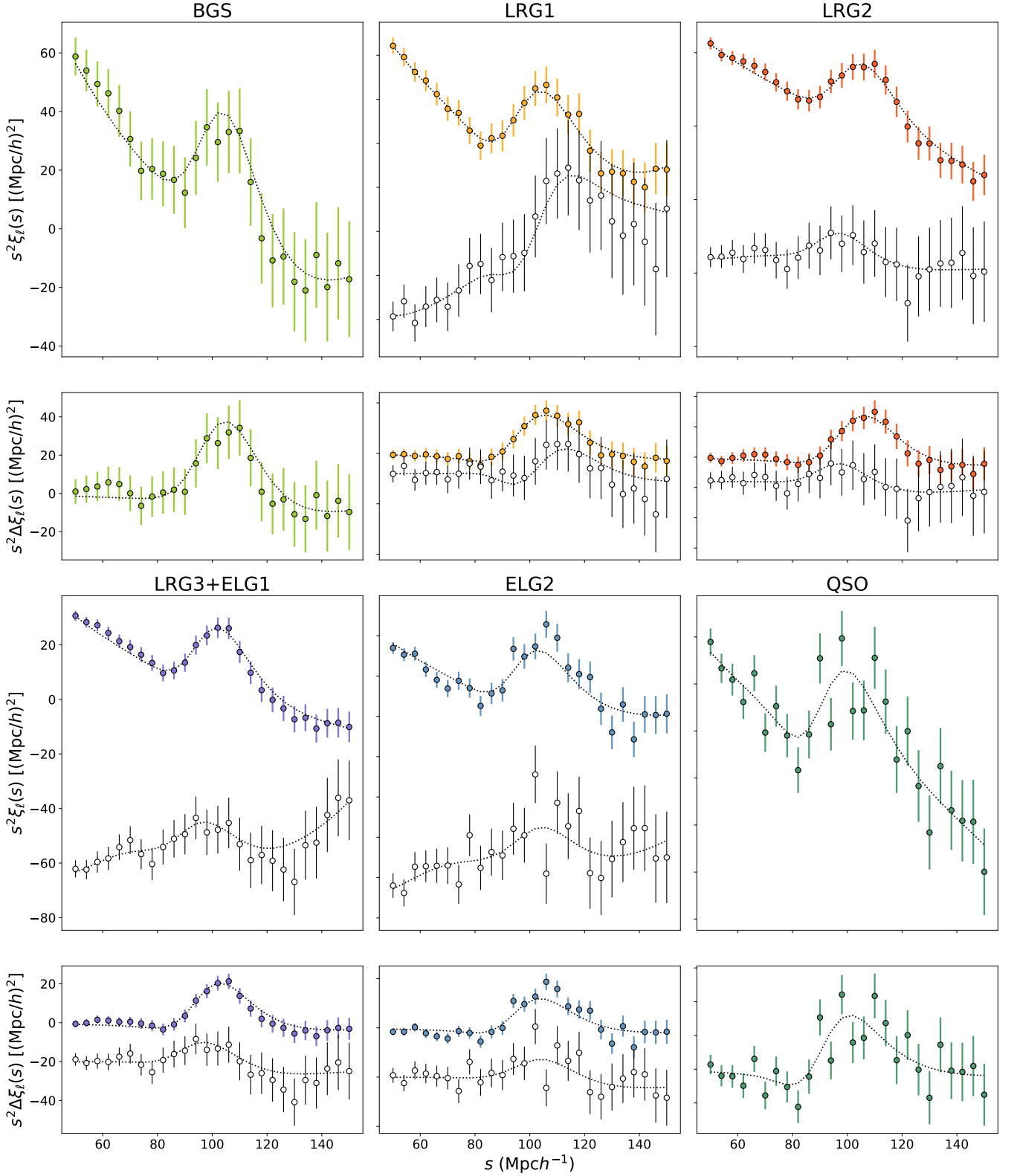


Figure 10. The best fit models for our the DESI tracers in the DR1 data with β_ϕ varying in the analysis, for comparison to the data. The coloured data shows the best fit models and data for the monopole, and the grey shows the quadrupole. The smaller panels show the isolated BAO peak for each tracer by subtracting the smooth model from the data. For visual clarity a small vertical offset has also been applied to the quadrupole for these panels.

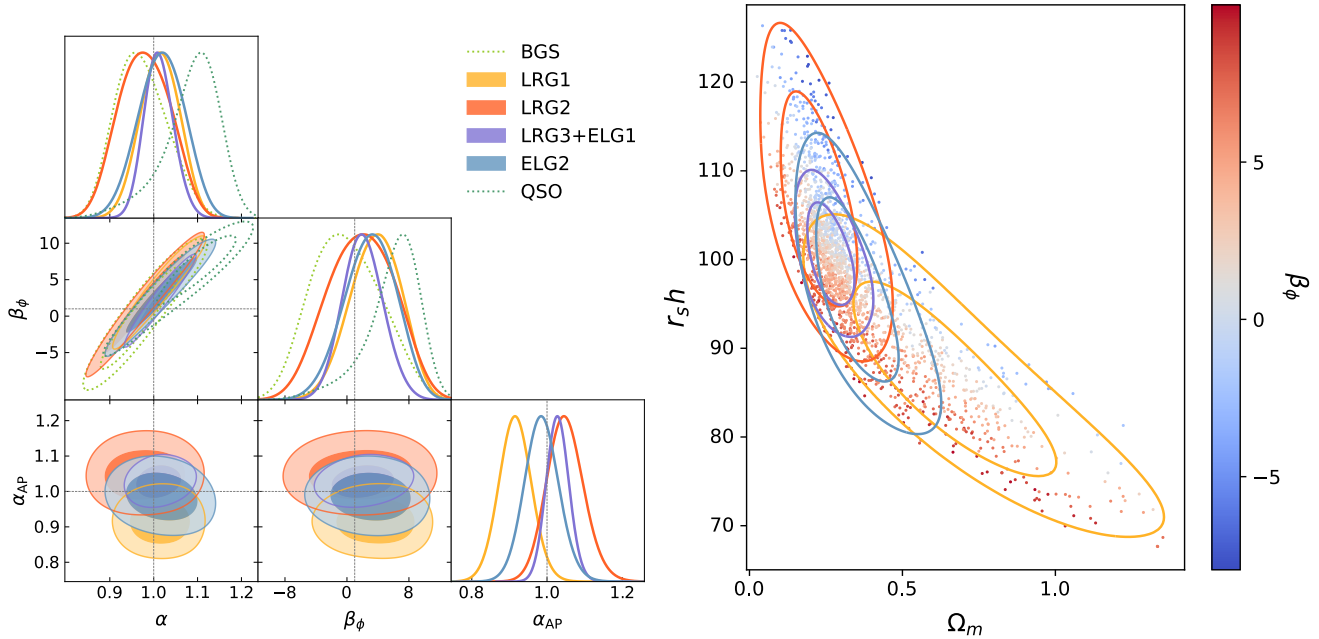


Figure 11. Left panel: contours for α , α_{AP} and β_ϕ for the baseline fits to the DESI DR1 data. The fits by QSOs and BGS which are not able to constrain β_ϕ well in the DR1 data are shown as dotted unfilled contours. Right panel: contours for Ω_m , $r_s h$ (Mpc) for the baseline fits to the DESI DR1 data, for individual tracers. The scatter points and colorbar show the value of β_ϕ which as a degeneracy with $r_s h$.

low ℓ + low E .¹³ In these cases, the combined fit for β_ϕ is obtained using the same method as previously (equation 28), but only after the individual posterior distribution function for each tracer bin has been importance sampled with the *Planck* data. In other words, we have computed a new combined posterior as

$$P_{\text{combined}}(\beta_\phi) \propto \prod_i \int d\alpha_i d\alpha_{\text{AP},i} P_i(\alpha_i, \alpha_{\text{AP},i}, \beta_\phi | \xi_i) \times P_{\text{Planck}}(\alpha_i, \alpha_{\text{AP},i} | \Omega_m, r_s h, w, N_{\text{eff}}), \quad (29)$$

in which Ω_m , $r_s h$, N_{eff} and w (the matter density, sound horizon, effective number of neutrino species and in some cases additional parameters such as the dark energy equation of state, EOS) are constrained by *Planck* and i is the set of DESI tracers. Generally for the Λ CDM case in which dark energy is a cosmological constant we assume the curvature density $\Omega_k = 0$ and $\Omega_\Lambda = 1 - \Omega_m$ where Ω_Λ drives the accelerated expansion of the Universe. Each density component has an EOS and this has w fixed to $w = -1$ for a cosmological constant. When adding our *Planck*-based priors we perform the same calculation as in equation 10 and equation 11, but not necessarily limited to the Λ CDM case (in which case there is no longer a unique mapping from cosmological to BAO parameters). We can allow for a model in which the EOS of dark energy varies and thus w is an additional free parameter. We also consider the case in which the dark energy EOS is parameterized by $w(a) = w_0 + w_a(1 - a)$ or when A_{lens} is a free parameter. This is discussed later in this section.

By including the additional information from *Planck* about Ω_m

and $r_s h$ for the Λ CDM + N_{eff} case, the uncertainty on α and α_{AP} is reduced for each tracer. Consequently, this allows for better constraints not only on α but on β_ϕ due to their strong degeneracy. This can be seen from the purple and pink dashed lines in the left-hand panel of Figure 12, where, interestingly, the best fit value for β_ϕ does not shift noticeably when the information from the *Planck* Λ CDM + N_{eff} chains as prior information, with or without lensing information included. In including information from the *Planck* chains, we do not fold in any explicit CMB information on N_{eff} in order to report only the constraining power available on β_ϕ from the physical shifting of the BAO wiggles; the constraints on N_{eff} from *Planck* include additional information on N_{eff} from the CMB that is degenerate with other cosmological parameters, in the same way that there are additional signals in the galaxy clustering beyond the BAO phase shift that can constrain N_{eff} (see Figures 1 and 2).

Table 8 lists our combined constraints on β_ϕ from the DESI DR1 BAO data, and when the chains have been importance sampled with *Planck* data. For the DESI data alone, the measurement of β_ϕ is consistent with unity within 1σ , and suggests $\beta_\phi > 0$ at $> 68\%$ confidence. Including the *Planck* prior on the BAO parameters (either with or without lensing) sharpens this constraint by a factor of ~ 3 while keeping the maximum posterior value fixed. This leads to a significant detection of a non-zero phase shift ($\beta_\phi > 0$ at $> 4\sigma$), but also leads to a constraint that prefers a value of $N_{\text{eff}} > 3.044$ at greater than 95% confidence. The maximum *a posteriori* value is also large enough that it would correspond to an unphysical value of N_{eff} , although we note that a wide range of N_{eff} is allowed given the non-linear mapping from this to β_ϕ .

At first glance this then seems to suggest a phase shift in the BAO that, when combined with the *Planck* prior, prefers either a larger number of effective relativistic species than predicted by the Standard Model, or the presence of other non-standard physics which introduces a phase shift in the BAO (e.g., non-standard neutrino physics, Kreisch et al. 2020; or non-adiabatic primordial density

¹³ This prior is *not* the same as the prior included earlier from *Planck* on N_{eff} . This prior is only for the case we want to include information that impacts the constraints on α and α_{AP} , and allow the BAO data alone to constrain β_ϕ . However we do only include information from *Planck* on α and α_{AP} from chains in with N_{eff} varies freely.

Table 8. Constraints on β_ϕ from the combined DESI DR1 BAO tracers, alongside cases when a prior on the BAO α parameters has been included from the *Planck* data by weighting the chains from the BAO fits. We also show the number of (Gaussian) σ away each best fit to β_ϕ is from zero ($N_{\text{eff}} = 0$) and unity ($N_{\text{eff}} = 3.044$).

Data	Ω_m	$r_s h$ (Mpc)	β_ϕ	$\Delta\sigma(\beta_\phi > 0)$	$\Delta\sigma(\beta_\phi > 1)$
DESI DR1 BAO	$0.263^{+0.046}_{-0.054}$	99.7 ± 3.2	2.70 ± 1.70	1.6	1.0
DESI DR1 BAO + <i>Planck</i> prior $\alpha, \alpha_{\text{AP}}$	$0.263^{+0.045}_{-0.054}$	99.7 ± 2.7	$2.70^{+0.60}_{-0.67}$	4.3	2.6
DESI DR1 BAO + <i>Planck</i> prior $\alpha, \alpha_{\text{AP}}$ w/ lensing	$0.263^{+0.045}_{-0.054}$	99.8 ± 2.7	$2.69^{+0.59}_{-0.66}$	4.3	2.7
DESI DR1 BAO + <i>Planck</i> prior $\alpha, \alpha_{\text{AP}}$ w/ varying A_{lens}	$0.265^{+0.046}_{-0.054}$	100.4 ± 2.7	2.05 ± 0.55	3.7	1.9
DESI DR1 BAO + <i>Planck</i> prior $\alpha, \alpha_{\text{AP}}$ w/ varying w	–	–	2.44 ± 0.70	3.4	2.0
DESI DR1 BAO + <i>Planck</i> prior $\alpha, \alpha_{\text{AP}}$ w/ varying w_0, w_a	–	–	$3.7^{+1.2}_{-1.1}$	3.2	2.3

fluctuations, [Baumann et al. 2016](#)). A similar finding was reported by [Baumann et al. \(2019\)](#) for the BOSS DR12 BAO data, who found $\beta_\phi = 1.2 \pm 1.8$ from combining two redshift bins, and $\beta_\phi = 2.22 \pm 0.75$ after including a prior from *Planck* by importance sampling. These two sets of results are remarkably consistent in central value and precision.

Compared to the fits from the BAO data alone or when priors from *Planck* are included in the fits, *Planck* alone prefers a larger Ω_m and smaller $r_s h$. The discrepancy in the best fit for Ω_m is slightly greater than the case for the fits to the BAO DR1 data fits when β_ϕ is fixed, in which case [Adame et al. \(2024b\)](#) reports $\Omega_m = 0.295 \pm 0.015$. However, when β_ϕ is free the data prefers a value for $r_s h$ which is lower but more consistent with the best fit from *Planck*. This may be related to the degeneracy that can be seen between $r_s h$ and β_ϕ in [Figure 12](#); this parameter degeneracy arises since both $r_s h$ and β_ϕ shift the BAO wiggles along the k -axis.

To investigate the impact of the *Planck* priors on the fits to β_ϕ further, we also followed the tests done in [Baumann et al. \(2019\)](#) and included a *Planck* prior for the Λ CDM model with A_{lens} (the lensing amplitude) allowed to be free in the analysis. We find a result $\beta_\phi = 2.05 \pm 0.55$, which is both a tighter constraint and closer to unity. The result is that our detection of a non-zero phase shift becomes now $> 3\sigma$, but the tension with the Standard Model prediction is reduced somewhat from 2.6 to 1.9σ . This fit is still consistent with the result from the BOSS DR12 data at the 1σ level.¹⁴

Lastly, while the *Planck* data does tend to increase the tension between our β_ϕ and the Standard Model prediction, the prior from *Planck* is based on chains from sampling in the Λ CDM model, while DESI data (in combination with CMB and Type Ia Supernovae) moderately prefer a $w_0 w_a$ CDM (time-varying Dark Energy) model ([Adame et al. 2024b](#)). Given that we are including a prior from a model that is not preferred by DESI constraints on the BAO scaling parameters, this might encourage the combined fit to β_ϕ from DESI with a Λ CDM *Planck* prior to take a higher than expected value of β_ϕ . As such we include fits from a full MCMC fit to a time-varying Dark Energy model with varying N_{eff} . We present results for the w CDM model (in which case we have the normal flat Λ CDM model + N_{eff} but w is allowed to vary as a single free parameter). We find this tends to allow the best fit value of β_ϕ to shift to a value that also reduces the tension with the standard model with $\beta_\phi = 2.44 \pm 0.70$. This may be due to the additional flexibility in the model. In the case for the time-varying EOS model $w_0 w_a$ CDM + N_{eff} , where the additional parameters w_0 and w_a vary in the EOS $w(a) = w_0 + (1 - a)w_a$, we find that the additional free parameters lead to weaker constraints

and has slightly greater tension with the theoretical expectation for N_{eff} , with $\beta_\phi = 3.7^{+1.2}_{-1.1}$.

5 CONCLUSION

In this work, we have applied the scheme derived in [Baumann et al. \(2019\)](#) to measure the phase shift in the BAOs. This phase shift is induced by free-streaming particles that propagate faster than the sound speed of the primordial plasma and thus allows one to measure the impact of free-streaming neutrinos that contribute to N_{eff} in the early Universe.

Compared to the analysis on BAOs by [Baumann et al. \(2019\)](#), we have extended the phase shift scheme for an anisotropic BAO fitting analysis, which we have applied to the DESI DR1 BAO data for galaxies and quasars. In the process, we have also extended the publicly available codes *desilike* to create the fits and likewise *Barry* to validate the fitting methodologies used between two separate codes. We tested our pipeline with *desilike* and *Barry* on highly precise cubic box simulations to ensure the robustness of the fitting schemes when applied to data with low statistical noise. Further to this we tested the pipeline and codes on realistic mocks for the various tracers in the DESI DR1 data release before applying the code to the real DR1 data.

Our analysis on the highly precise cubic box simulations has highlighted the need to address systematics in the BAO fitting methodology for future constraints with the 5 year DESI data. Further investigation will be required in order to determine a more robust way to measure the phase shift for different broadband fitting methodologies for the power spectrum. We also expect there may be a need to address other differences seen in the fits when varying the analysis pipeline if the measurements of the BAO distortion parameters and β_ϕ are larger relative to a reduced statistical uncertainty in future measurements. Potentially, it will also be necessary to consider in greater detail the impact of the choice of fiducial cosmology or template cosmology. Further to this, while allowing β_ϕ to vary significantly weakens constraints on α due to the strong degeneracy between these parameters, it may be interesting to consider where fixing β_ϕ could lead to small biases in α , particularly as we continue to report more precise measurements with upcoming data from DESI.

We have measured the phase shift in the DR1 DESI data from the combination of LRGs and ELGs across various redshift bins to be $\beta_\phi = 2.7 \pm 1.7$. This is larger than the measurement of $\beta_\phi = 1.2 \pm 1.8$ in [Baumann et al. \(2019\)](#), however both measurements agree within the 1σ uncertainties. When we add a prior on α and α_{AP} from *Planck* 2018 measurements of the CMB, we obtain $\beta_\phi = 2.7^{+0.60}_{-0.67}$, which as before is larger than the value of 2.22 ± 0.75 given in [Baumann et al. \(2019\)](#) with the same prior included. In cosmological models with

¹⁴ ([Baumann et al. 2019](#)) find $\beta_\phi = 1.53 \pm 0.83$ for Λ CDM + N_{eff} + A_{lens} .

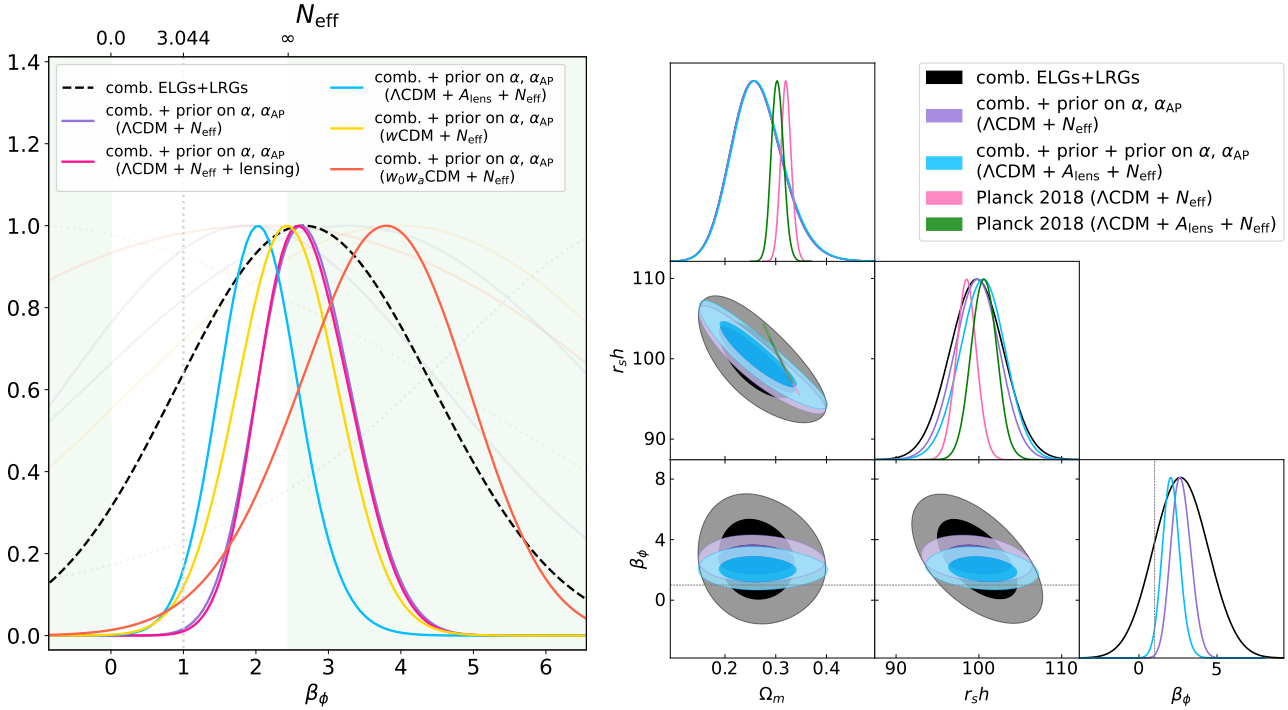


Figure 12. Left panel: the 1D posterior fits for β_ϕ , including a combined fit to the tracers (excluding BGS and QSOs, black dashed line), and various combined fits when a CMB prior for α and α_{AP} has been included by importance sampling (corresponding to the fits shown in Table 8). The priors all use fits to the *Planck* chains for TT+TE+EE + low ℓ + lowE. We include a prior from fits to Λ CDM + N_{eff} (purple, dashed line), the same but with lensing information included (pink, dashed), the case for a Λ CDM prior (blue), Λ CDM + A_{lens} (red) and finally wCDM (orange). The faint lines show the 1D posteriors of β_ϕ for each tracer that are shown in Figure 11. Right panel: a combined fit for Ω_m , $r_s h$ and β_ϕ to three LRG bins and the ELG2 bin is shown as a black contour. The fits by QSOs and BGS are not included here. We also show the fits when each tracer has a CMB prior for α and α_{AP} by importance sampling using the *Planck* chains for fits to TT+TE+EE + low ℓ + lowE in the context of Λ CDM + N_{eff} . For comparison the *Planck* chains are also shown for just Ω_m and $r_s h$.

only Standard Model particles the phase shift can be interpreted as due to N_{eff} . However here the phase shift measurements of $\beta_\phi \geq 2.44$ do not correspond to a physical value for N_{eff} . The amplitude of the phase shift may hint at physics beyond the standard model since it is not entirely consistent with an interpretation via N_{eff} . However, we emphasize here that the measurement of β_ϕ is for a physical phase shift that is present in the BAOs, and in a non-standard model could be impacted by non-standard neutrino physics (Kreisch et al. 2020) or by non-adiabatic fluctuations (Baumann et al. 2016). Furthermore, our measurements of β_ϕ from DESI BAOs alone are still consistent with physical values of N_{eff} at the 1σ level.

In the future, the analysis can potentially be applied to the DESI Y3 or DESI Y5 data. Baumann et al. (2019) forecasts that with the DESI Y5 data it may be potential to obtain $\sigma(\beta_\phi) \sim 0.3$, which is a factor of ~ 6 better than the constraints reported here for the BAO only data, although these forecasts may not include the impact of allowing α_{AP} to vary freely as is done in this work. In order to provide competitive constraints on future data with DESI Y5, it will be necessary to begin to improve the systematics on our measurements that were analysed in detail in section 3.

In future work, it will also be interesting to consider the impact of a phase shift due to particles that may have different properties to Standard Model neutrinos, such as interacting neutrinos. It may be expected that such neutrinos could change the functional form of the phase shift that is given by equation 17 due to the fact that neutrino interactions can change the epoch of free-streaming (Kreisch et al. 2020; Camarena et al. 2023). This may be particularly interesting in the future when stronger constraints on β_ϕ are possible, particularly

in light of results that find a bimodal distribution for a parameter that characterises the interaction strength of strongly interacting neutrinos (Camarena et al. 2023; Kreisch et al. 2024). It may also be interesting for future work to consider the ability of DESI+*Planck* to constrain the phase shift in the context of more models beyond Λ CDM, or consider adding information from CMB probes for the phase shift induced by free-streaming relics, such as the constraints found by Follin et al. (2015).

ACKNOWLEDGEMENTS

This research has made use of NASA’s Astrophysics Data System bibliographic services, the astro-ph pre-print archive at <https://arxiv.org/> and the python libraries MATPLOTLIB, GETDIST, CHAINCONSUMER, NUMPY, SCIPY and PANDAS (Hunter & Dale 2007; Lewis 2019; Hinton 2016; Harris et al. 2020; Virtanen et al. 2020; Wes McKinney 2010).

This material is based upon work supported by the U.S. Department of Energy (DOE), Office of Science, Office of High-Energy Physics, under Contract No. DE-AC02-05CH11231, and by the National Energy Research Scientific Computing Center, a DOE Office of Science User Facility under the same contract. Additional support for DESI was provided by the U.S. National Science Foundation (NSF), Division of Astronomical Sciences under Contract No. AST-0950945 to the NSF’s National Optical-Infrared Astronomy Research Laboratory; the Science and Technology Facilities Council of the United Kingdom; the Gordon

and Betty Moore Foundation; the Heising-Simons Foundation; the French Alternative Energies and Atomic Energy Commission (CEA); the National Council of Humanities, Science and Technology of Mexico (CONACYT); the Ministry of Science, Innovation and Universities of Spain (MICIU/AEI/10.13039/501100011033), and by the DESI Member Institutions: <https://www.desi.lbl.gov/collaborating-institutions>. Any opinions, findings, and conclusions or recommendations expressed in this material are those of the author(s) and do not necessarily reflect the views of the U. S. National Science Foundation, the U. S. Department of Energy, or any of the listed funding agencies.

The authors are honored to be permitted to conduct scientific research on Iolkam Du’ag (Kitt Peak), a mountain with particular significance to the Tohono O’odham Nation.

This work used the DiRAC@Durham facility managed by the Institute for Computational Cosmology on behalf of the STFC DiRAC HPC Facility (www.dirac.ac.uk). The equipment was funded by BEIS capital funding via STFC capital grants ST/K00042X/1, ST/P002293/1, ST/R002371/1 and ST/S002502/1, Durham University and STFC operations grant ST/R000832/1. DiRAC is part of the National e-Infrastructure.

The authors thank Willem Elbers for providing full MCMC fits to the *Planck* 2018 data for various cosmological models. The authors also thank Willem Elbers, Ariel Sanchez and Seshadri Nadathur for their substantial feedback that has helped to improve the writing of this paper. AW thanks David Camarena for interesting discussion, facilitated by the Galileo Galilei Institute of Theoretical Physics in Florence, Italy at the *Neutrino Frontiers* workshop in 2024. AW, TD and CH acknowledge support from the Australian Government through the Australian Research Council’s Laureate Fellowship funding scheme (FL180100168). HR, MV, and SF are supported by PAPIIT IN108321, PAPIIT IN116024, and PAPIIT IN115424.

DATA AVAILABILITY

The data will be publicly available once the paper is accepted for publication. The code used to produce fits with *Barry*, including modifications for the phase shift amplitude, is available at <https://github.com/abbew25/Barry>. The *desilike* code to produce fits with the phase shift amplitude can be accessed at <https://github.com/cosmodesi/desilike>.

REFERENCES

Abbott T., et al., 2019, *Monthly Notices of the Royal Astronomical Society*, 483, 4866
 Adame A., et al., 2024a, arXiv preprint arXiv:2404.03000
 Adame A., et al., 2024b, arXiv preprint arXiv:2404.03002
 Aghamousa A., et al., 2016, arXiv preprint arXiv:1611.00036
 Aghanim N., et al., 2020, *Astronomy & Astrophysics*, 641, A6
 Alcock C., Paczyński B., 1979, *Nature*, 281
 Bashinsky S., Seljak U., 2004, *Phys. Rev. D*, 69
 Baumann D., Green D., Meyers J., Wallisch B., 2016, *Journal of Cosmology and Astroparticle Physics*, 2016, 007
 Baumann D., Green D., Wallisch B., 2018, *Journal of Cosmology and Astroparticle Physics*, 2018, 029
 Baumann D., Beutler F., Flauger R., Green D., Slosar A., Vargas-Magaña M., Wallisch B., Yeche C., 2019, *Nature Physics*, 15, 465
 Bernal J. L., Smith T. L., Boddy K. K., Kamionkowski M., 2020, *Physical Review D*, 102, 123515
 Beutler F., et al., 2017, *Monthly Notices of the Royal Astronomical Society*, 466, 2242

Blas D., Lesgourgues J., Tram T., 2011, *Journal of Cosmology and Astroparticle Physics*, 2011, 034
 Camarena D., Cyr-Racine F.-Y., Houghteling J., 2023, *Physical Review D*, 108, 103535
 Chen S.-F., et al., 2024, arXiv preprint arXiv:2402.14070
 Chuang C.-H., Kitaura F.-S., Prada F., Zhao C., Yepes G., 2015, *Monthly Notices of the Royal Astronomical Society*, 446, 2621
 Cole S., et al., 2005, *Monthly Notices of the Royal Astronomical Society*, 362, 505
 Eisenstein D. J., et al., 2005, *The Astrophysical Journal*, 633, 560
 Follin B., Knox L., Millea M., Pan Z., 2015, *Physical Review Letters*, 115, 091301
 Foreman-Mackey D., Hogg D. W., Lang D., Goodman J., 2013, *Publications of the Astronomical Society of the Pacific*, 125, 306
 Garcia-Quintero C., et al., 2024, arXiv preprint arXiv:2404.03009
 Gil-Marín H., et al., 2016, *Monthly Notices of the Royal Astronomical Society*, 460, 4210
 Hadzhiyska B., et al., 2023, arXiv preprint arXiv:2308.12343
 Harris C. R., et al., 2020, *Nature*, 585, 357
 Hartlap J., Simon P., Schneider P., 2007, *Astronomy & Astrophysics*, 464, 399
 Hinton S. R., 2016, *The Journal of Open Source Software*, 1, 00045
 Hinton S. R., et al., 2016, *Monthly Notices of the Royal Astronomical Society*, p. stw2725
 Hinton S. R., Howlett C., Davis T. M., 2020, *Monthly Notices of the Royal Astronomical Society*, 493, 4078
 Hunter J., Dale D., 2007, *Matplotlib 0.90.0 user’s guide*
 Jackson J., 1972, *Monthly Notices of the Royal Astronomical Society*, 156, 1P
 Kaiser N., 1987, *Monthly Notices of the Royal Astronomical Society*, 227, 1
 Kreisch C. D., Cyr-Racine F.-Y., Doré O., 2020, *Physical Review D*, 101, 123505
 Kreisch C. D., et al., 2024, *Physical Review D*, 109, 043501
 Lange J. U., 2023, *Monthly Notices of the Royal Astronomical Society*, 525, 3181
 Lewis A., 2019, arXiv preprint arXiv:1910.13970
 Maksimova N. A., Garrison L. H., Eisenstein D. J., Hadzhiyska B., Bose S., Satterthwaite T. P., 2021, *Monthly Notices of the Royal Astronomical Society*, 508, 4017
 Mena-Fernandez J., et al., 2024, arXiv preprint arXiv:2404.03008
 Moon J., et al., 2023, *Monthly Notices of the Royal Astronomical Society*, 525, 5406
 O. Alves et al. 2024, in preparation
 Paillas E., et al., 2024, arXiv preprint arXiv:2404.03005
 Penzias A. A., Wilson R. W., 1979, in , *A Source Book in Astronomy and Astrophysics, 1900–1975*. Harvard University Press, pp 873–876
 Percival W. J., et al., 2014, *Monthly Notices of the Royal Astronomical Society*, 439, 2531
 Percival W. J., Friedrich O., Sellentin E., Heavens A., 2022, *Monthly Notices of the Royal Astronomical Society*, 510, 3207
 Pérez-Fernández A., et al., 2024, arXiv preprint arXiv:2406.06085
 Philcox O. H., Eisenstein D. J., O’Connell R., Wiegand A., 2020, *Monthly Notices of the Royal Astronomical Society*, 491, 3290
 Rashkovetskyi M., et al., 2024, arXiv preprint arXiv:2404.03007
 Rocher A., et al., 2023, *Journal of Cosmology and Astroparticle Physics*, 2023, 016
 Vargas-Magaña M., et al., 2018, *Monthly Notices of the Royal Astronomical Society*, 477, 1153–1188
 Virtanen P., et al., 2020, *Nature Methods*, 17, 261
 Wadekar D., Scoccimarro R., 2020, *Physical Review D*, 102, 123517
 Wes McKinney 2010, in Stéfan van der Walt Jarrod Millman eds, *Proceedings of the 9th Python in Science Conference*. pp 56 – 61, doi:10.25080/Majora-92bf1922-00a
 Yuan S., et al., 2024, *Monthly Notices of the Royal Astronomical Society*, 530, 947

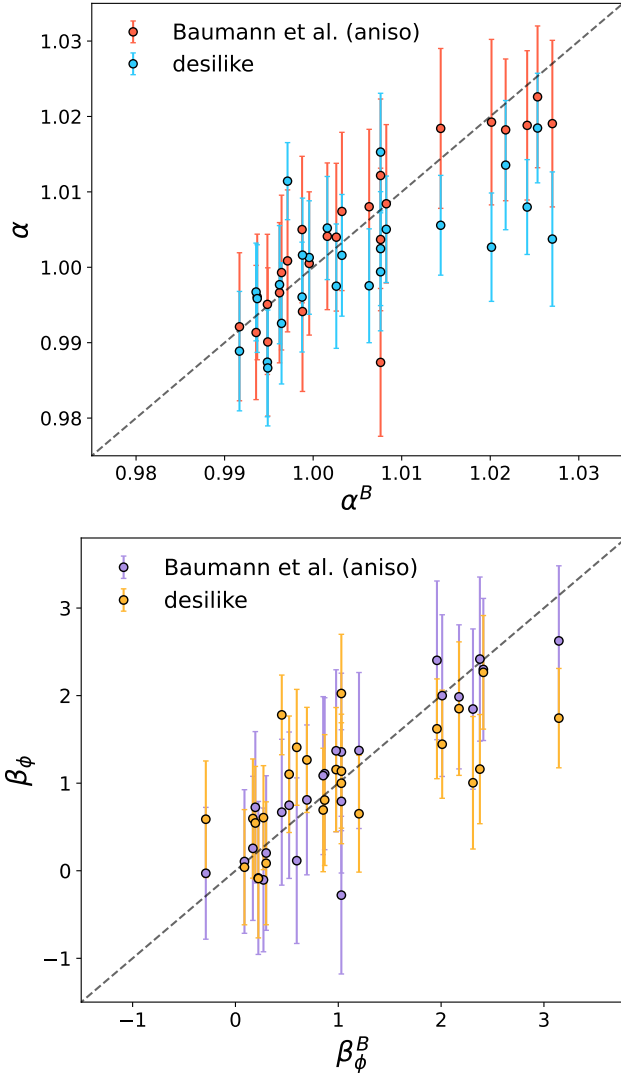
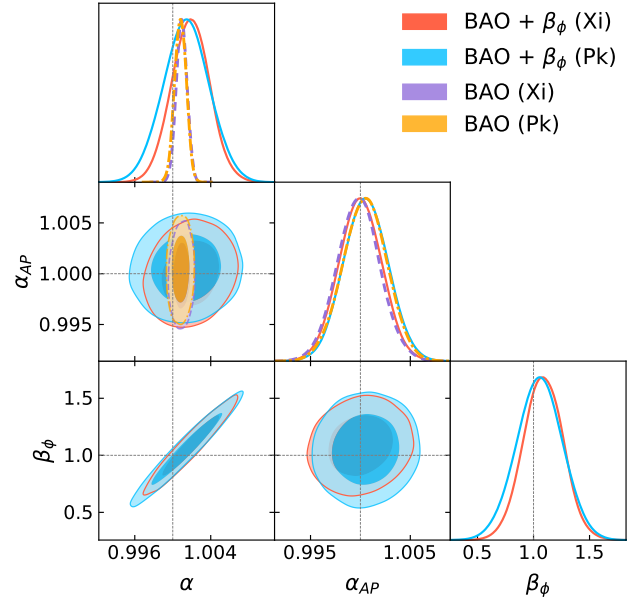


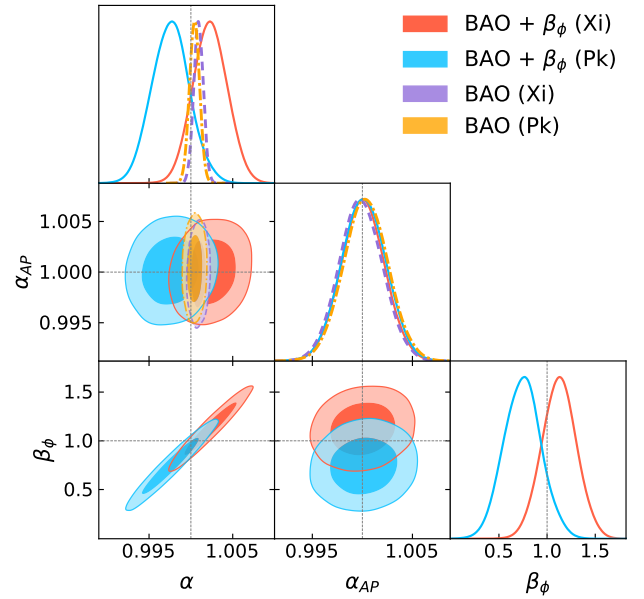
Figure A1. Results of fitting α (top panel) and β_ϕ (lower panel) for 25 mock realisations using the Pipeline of [Baumann et al. \(2019\)](#), compared to an extended version of the Baumann pipeline for anisotropic fitting, and additionally comparing to the *desilike* pipeline.

APPENDIX A: VALIDATING THE ANISOTROPIC PIPELINE BY COMPARISON TO BAUMANN ET AL (2019)

We show the fits produced by following the isotropic BAO pipeline by [Baumann et al. \(2019\)](#) with β_ϕ allowed to vary. Fits were produced in configuration space, and compared to the results from the *desilike* pipeline (following an anisotropic fitting scheme) and an extended version of the approach of [Baumann et al. \(2019\)](#) for an anisotropic fitting scheme. The pipeline of [Baumann et al. \(2019\)](#) in configuration space uses a minimizer to find the best fit. The errors on the fits are evaluated by calculating the χ^2 on a grid in $\{\alpha, \beta_\phi\}$ parameters to map out the likelihood surface. The anisotropic extension of this scheme calculates the best fit in a similar way but extends the parameter space to $\{\alpha, \beta_\phi, \alpha_{AP}\}$. The approach by [Baumann et al. \(2019\)](#) uses the nonlinear model for the correlation function described in [Vargas-Magaña et al. \(2018\)](#). However in their work, the Fourier-space fits use the same modelling as this work, following the methodology of [Beutler et al. \(2017\)](#). The results of the fits from each code are compared in [Figure A1](#).



(a) Our fits with spline broadband method.



(b) Our fits with polynomial broadband method.

Figure B1. Comparison of the power spectrum and correlation function, for standard BAO fits with CV ELGs (first-generation snapshots at $z = 1.1$) and for fits when the phase shift is varied. Here however, we show the difference when the spline broadband methodology is used.

APPENDIX B: ADDITIONAL COMPARISONS FROM BARRY

In [Figure B1](#) we show an additional fit for the mock mean of the first-generation control-variate mocks for ELGs with $z = 1.1$, to compare the power spectrum and correlation function fits for the two broadband methodologies, and also to compare the results to the standard BAO fitting procedure.

This paper has been typeset from a $\text{\TeX}/\text{\LaTeX}$ file prepared by the author.